

Vitorino Biazzi Neto

**FBG-based sensing systems for robotic  
manipulators to monitor interactions in  
unstructured environments**

Vitória, ES

March 2022



Vitorino Biazi Neto

# **FBG-based sensing systems for robotic manipulators to monitor interactions in unstructured environments**

Dissertation submitted to the Graduate Program in Electrical Engineering of the Technology Center of the Federal University of Espírito Santo as partial requirement for obtaining the Master's Degree in Electrical Engineering.

Federal University of Espírito Santo

Technology Center

Graduate Program in Electrical Engineering

Supervisor: Prof. Dr. Arnaldo Gomes Leal Junior

Co-supervisor: Prof. Dr. Anselmo Frizera Neto

Vitória, ES

March 2022

Ficha catalográfica disponibilizada pelo Sistema Integrado de  
Bibliotecas - SIBI/UFES e elaborada pelo autor

---

B576f      Biazi Neto, Vitorino, 1995-  
            FBG-based sensing systems for robotic manipulators to  
            monitor interactions in unstructured environments / Vitorino  
            Biazi Neto. - 2022.  
            88 f. : il.

            Orientador: Arnaldo Gomes Leal Junior.  
            Coorientador: Anselmo Frizera Neto.  
            Dissertação (Mestrado em Engenharia Elétrica) -  
            Universidade Federal do Espírito Santo, Centro Tecnológico.

            1. Fiber Bragg Grating. 2. optical sensors. 3. robotic  
            manipulators. I. Gomes Leal Junior, Arnaldo. II. Frizera Neto,  
            Anselmo. III. Universidade Federal do Espírito Santo. Centro  
            Tecnológico. IV. Título.

CDU: 621.3

---

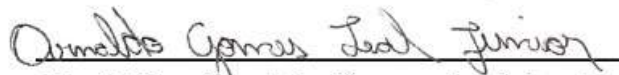


Vitorino Biazi Neto

## **FBG-based sensing systems for robotic manipulators to monitor interactions in unstructured environments**

Dissertation submitted to the Graduate Program in Electrical Engineering of the Technology Center of the Federal University of Espírito Santo as partial requirement for obtaining the Master's Degree in Electrical Engineering.

Dissertation approved. Vitória, ES, March 14th, 2022:



**Prof. Dr. Arnaldo Gomes Leal Junior**

Advisor


Graduate Program in Electrical Engineering  
Federal University of Espírito Santo



**Prof. Dr. Anselmo Frizera Neto**

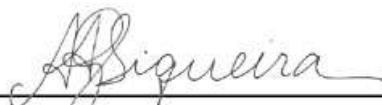
Co-advisor

Graduate Program in Electrical Engineering  
Federal University of Espírito Santo



**Prof Dr. Maria José Pontes**

Graduate Program in Electrical Engineering  
Federal University of Espírito Santo



**Prof. Dr. Adriano Almeida Gonçalves  
Siqueira**

Engineering School of São Carlos  
University of São Paulo

Vitória, ES  
March 2022



# Acknowledgements

First, I would like to thank my family for being my support in my entire life. I would like to thank my father Sergio, my mother Rosa and my brother and sisters, Sergio Junior, Carolina and Maria Vitoria, for all the affection and for always believing in all my dreams. I wouldn't make this far without you.

I thank my girlfriend, Jessica, for being my best company in these years and a very important person in my life. Thank you for being by my side in difficult times and supporting me not to give up. I am so grateful for how much you are a part of my life.

I would like to thank all my friends and all other colleagues from the research group for all the technical and life teachings in these years of coexistence. A part of who I am is thanks to you.

I also thank my advisors, Prof. Dr. Arnaldo Leal Junior and Prof. Dr. Anselmo Frizera Neto, for all the academic knowledge acquired on this journey, for their availability to always help me, and for all the opportunities that were given to me.

I would like to express my gratitude to my master's internship supervisor, Dr. Carlos Marques, for the incredible opportunity to work temporarily in his research group at the University of Aveiro in Portugal. Thanks for the amazing reception and support in those months. In addition, I would like to thank the entire i3N group.

Finally, I thank the Graduate Program in Electrical Engineering and the LABTEL at the Federal University of Espirito Santo for the technical support and the CNPq for the financial support.

This research is financed by FAPES (320/2020, 84336650 and 197/2021) and CNPq (304049/2019-0).



*“Foi o tempo que dedicaste à tua rosa que a fez tão importante.”  
(Antoine de Saint-Exupéry)*



# Abstract

The emergence of Industry 4.0 has brought new concepts to the factories that optimize and improve conventional processes. These technologies have brought assignments to the industrial robots that allow them to perform tasks faster and more precisely. The improvement of the robot's proprioception capacity and tactile sensitivity through the use of sensors is a useful approach to achieve those goals. Optical fibers are a viable technology to be used as sensors in robotic devices because they are electrically passive and present electromagnetic immunity. This dissertation proposes two Fiber Bragg Grating (FBG) based sensing systems to monitor robotic manipulators during their operation. The first system are instrumented claws which work based on the strain rosette strategy to measure the critical stress-strain state on its surface while an object is being picked up. The other one consists of a group of smart textiles installed on the robot's body to detect interactions with the environment. Three FBG sensors are positioned according to a strain rosette configuration within a slot in two 3D printed claws. The equations based on elasticity theory to obtain the stress-strain state from the sensors data are developed and a methodology using an auxiliary temperature sensor to prevent cross-sensitivity and to avoid measurement errors is proposed. The characterization tests show a highly linear behavior in terms of sensitivity to strain ( $R^2 = 0.996$  for the linear regression of the means) and to temperature variation (lower  $R^2$  between FBGs equal to 0.9868). From the compression tests, it is possible to conclude that the dynamic range of the sensors is adequate to the load capacity of the claws. Grip tests with different objects were performed on the manipulator to verify the system's feasibility in real-time applications. The tactile system consists of a group of optical fibers with multiplexed FBGs embedded in silicone rubber. The optical fibers with the sensors are positioned between layers of polyethylene foam and cotton fabric. A mathematical model is proposed to determine the maximum distance between FBGs on the system to achieve the system's best spatial resolution. After the manufacturing process, temperature and force characterization presents almost all values of  $R^2$  on the linear regression superior to 0.94. Individual analysis are performed for the sensors which presented low coefficient of determination. Finally, on the experimental validation of the system, it can be observed that it can provide the position on robot's body, the amplitude in terms of force and instant of time which a external impact occurred.

**Keywords:** Fiber Bragg Grating. optical sensors. robotic manipulators.





# Resumo

O surgimento da Indústria 4.0 trouxe novos conceitos para as fábricas que otimizaram e aprimoraram os processos convencionais. Essas tecnologias trouxeram atribuições aos robôs industriais que lhes permitem realizar tarefas com mais rapidez e precisão. A melhoria da capacidade proprioceptiva e da sensibilidade tátil do robô por meio do uso de sensores é uma abordagem útil para atingir esses objetivos. As fibras ópticas são uma tecnologia viável para serem utilizadas como sensores em dispositivos robóticos, pois são eletricamente passivas e possuem imunidade eletromagnética. Esta dissertação propõe dois sistemas de sensoriamento baseados em Redes de Bragg (FBG, do inglês *Fiber Bragg Grating*) para monitorar manipuladores robóticos durante sua operação. O primeiro sistema são garras instrumentadas que funcionam com base na estratégia de rosetas de deformação para medir o estado crítico de tensão-deformação em sua superfície enquanto um objeto está sendo capturado. O outro sistema consiste em um grupo de tecidos inteligentes instalados no corpo do robô para detectar interações com o ambiente. Três sensores FBG são posicionados de acordo com uma configuração de roseta de deformação dentro de um rasgo em duas garras impressas em 3D. Equações baseadas na teoria da elasticidade para obter o estado tensão-deformação a partir dos dados dos sensores são desenvolvidas e é proposta uma metodologia utilizando um sensor auxiliar de temperatura para evitar efeitos de sensibilidade cruzada e erros de medição. Os testes de caracterização mostram um comportamento altamente linear em termos de sensibilidade à deformação ( $R^2 = 0,996$  para a regressão linear das médias) e à variação de temperatura (menor  $R^2$  entre FBGs igual a 0,9868). A partir dos ensaios de compressão, é possível concluir que a faixa dinâmica dos sensores é adequada à capacidade de carga das garras. Testes de aperto com diferentes objetos foram realizados no manipulador para verificar a viabilidade do sistema em aplicações em tempo real. O sistema tátil consiste em um grupo de fibras ópticas com FBGs multiplexadas, embutidas em borracha de silicone. As fibras ópticas com os sensores são posicionadas entre camadas de espuma de polietileno e tecido de algodão. Um modelo matemático é proposto para determinar a distância máxima entre FBGs no sistema a fim de alcançar a melhor resolução espacial do sistema. Após o processo de fabricação, a caracterização de temperatura e força apresenta quase todos os valores de  $R^2$  na regressão linear superiores a 0,94. Análises individuais são feitas para os sensores que apresentaram baixo coeficiente de determinação. Por fim, na validação experimental do sistema, pode-se observar que ele pode fornecer a posição no corpo do robô, a amplitude em termos de força e instante de tempo em que ocorreu um impacto externo.

**Palavras-chave:** Redes de Bragg. sensores ópticos. manipuladores robóticos.



# List of Figures

Figure 1 – Manipulators with (a) open kinematic chain and (b) closed kinematic chain. (SICILIANO et al., 2010) . . . . .	27
Figure 2 – Representation of a manipulator (a) inverse kinematics and (b) dynamics (CRAIG, 2009). . . . .	29
Figure 3 – Some of the strain rosette configurations: (a) Y, (b) rectangular and (c) delta. . . . .	31
Figure 4 – Strain elements oriented to (a) principal strains and (b) maximum shear strain. . . . .	32
Figure 5 – Strain rosette parameters for (a) Y, (b) rectangular and (c) delta configurations. . . . .	34
Figure 6 – Scheme of the light propagation on the optical fiber. . . . .	36
Figure 7 – Scheme of the FBG working principle. . . . .	38
Figure 8 – Proposed sensing systems installed on the robot's body being (a) instrumented claws and (b) tactile system . . . . .	42
Figure 9 – (a) Robo Kuka KR3 R540 and (b) Elettric gripper LEHZ20 . . . . .	43
Figure 10 – Phase mask technique for inscription of FBGs (a) schematic and (b) laboratory setup. . . . .	44
Figure 11 – Claw front, superior, lateral and isometric views. . . . .	45
Figure 12 – (a) 3D printer Sigma R19 and (b) Positions of the FBGs on the claw. . . . .	46
Figure 13 – Second claw (a) 3D design and (b) manufactured prototype. . . . .	47
Figure 14 – Boundary conditions (a) distributed pressure and (b) fixed support. . . . .	47
Figure 15 – Experimental setup for FBGs characterization to temperature variation. . . . .	49
Figure 16 – Experimental setup for FBGs characterization to axial strain. . . . .	50
Figure 17 – Experimental setup of the compression tests. . . . .	51
Figure 18 – Claws sensing system installed on the robot. . . . .	52
Figure 19 – Data collection points in instrumented claws validation experiments (a) point 0, (b) point 1 and (c) point 2. . . . .	53
Figure 20 – Coordinate systems on (a) the left claw and (b) the right claw. . . . .	54
Figure 21 – Parameter of the simply supported beam with a concentrated load. . . . .	55
Figure 22 – Representation of the fiber undergoing a transversal deformation. . . . .	57
Figure 23 – Nomenclature used for the smart textiles and FBGs installed on the robot's body. . . . .	59
Figure 24 – Internal components that make up the smart textiles. . . . .	60
Figure 25 – Universal test machine for the force characterization experiments. . . . .	61
Figure 26 – Tactile sensing system installed on the robot. . . . .	62

Figure 27 – Strain field on the epoxy resin from FEM simulation for (a) FBG 1, (b) FBG 2 and (c) FBG 3. . . . .	63
Figure 28 – Temperature characterization of the FBGs from the first design for (a) left claw and (b) right claw. . . . .	64
Figure 29 – Temperature characterization of the FBGs from the second design for (a) left claw and (b) right claw. . . . .	65
Figure 30 – Characterization of the reference FBG relative to strain for the claws first design. . . . .	66
Figure 31 – Characterization relative to strain of the FBGs for left claw of second design . . . . .	67
Figure 32 – Characterization relative to strain of the FBGs for right claw of second design. . . . .	67
Figure 33 – Strain values for compression test on the first design for (a) left claw and (b) right claw. . . . .	68
Figure 34 – Reflection spectrum of FBG 3 (right claw) under compressive load. . .	69
Figure 35 – Strain values for compression test on the second design for (a) left claw and (b) right claw. . . . .	70
Figure 36 – Temperature characterization of smart textiles in relation to (a) link 1, (b) link 2, (c) link 3 and (d) link 4. . . . .	73
Figure 37 – Force characterization of smart textiles in relation to (a) link 1, (b) link 2, (c) link 3 and (d) link 4. . . . .	74
Figure 38 – Sensors response during the test of the tactile system without external perturbations. . . . .	76
Figure 39 – Sensors response during the test with hits on the left side of the robot's body. . . . .	77
Figure 40 – Sensors response during the test with hits on the front side of the robot's body. . . . .	77

# List of Tables

Table 1 – Mechanical properties of the materials from numerical analysis . . . . .	48
Table 2 – Optical fiber characteristics for estimating the distance between FBGs .	58
Table 3 – Results of the tests on the quadrangular prism. . . . .	72
Table 4 – Results of the tests on the cylinder. . . . .	72
Table 5 – Sensitivities of the tactile system sensors. . . . .	74



# List of abbreviations and acronyms

APC	Angled Physical Contact
ANN	Artificial Neural Network
CIM	Computer Integrated Manufacturing
DoF	Degrees of Freedom
FBG	Fiber Bragg Grating
FEM	Finite Element Method
FWHM	Full Width Half Maximum
IoT	Internet of Things
LCD	Liquid Crystal Display
MIS	Minimally Invasive Surgery
MIRS	Minimally Invasive Robotic Surgery
PLA	Polylactic Acid
POF	Polymeric Optical Fiber
POFBG	Polymeric Optical Fiber Bragg Grating
SAR	Socially Assistive Robotics
SLA	Stereolithography
UV	Ultraviolet





# Contents

<b>1</b>	<b>INTRODUCTION . . . . .</b>	<b>21</b>
<b>1.1</b>	<b>Motivation and justification . . . . .</b>	<b>21</b>
<b>1.2</b>	<b>Objectives . . . . .</b>	<b>24</b>
<b>1.3</b>	<b>Contributions . . . . .</b>	<b>25</b>
<b>1.4</b>	<b>Publications . . . . .</b>	<b>25</b>
<b>1.5</b>	<b>Dissertation Structure . . . . .</b>	<b>26</b>
<b>2</b>	<b>THEORETICAL BACKGROUND . . . . .</b>	<b>27</b>
<b>2.1</b>	<b>Robotic Manipulators . . . . .</b>	<b>27</b>
<b>2.2</b>	<b>Strain gauges and strain rosettes . . . . .</b>	<b>30</b>
<b>2.3</b>	<b>Optical Fiber Overview . . . . .</b>	<b>35</b>
<b>2.4</b>	<b>Fiber Bragg Grating . . . . .</b>	<b>37</b>
<b>3</b>	<b>MATERIAL AND METHODS . . . . .</b>	<b>41</b>
<b>3.1</b>	<b>Briefly introduction of the sensors systems . . . . .</b>	<b>41</b>
<b>3.2</b>	<b>Test environment presentation . . . . .</b>	<b>42</b>
<b>3.3</b>	<b>Sensors' description and manufacturing setup . . . . .</b>	<b>43</b>
<b>3.4</b>	<b>Instrumented claws' development . . . . .</b>	<b>44</b>
3.4.1	First prototype of the claws . . . . .	44
3.4.2	Second prototype of the claws . . . . .	46
3.4.3	FEM simulation . . . . .	47
3.4.4	Temperature and strain characterization . . . . .	48
3.4.5	Compression tests . . . . .	51
3.4.6	Experimental validation . . . . .	52
<b>3.5</b>	<b>Tactile system's development . . . . .</b>	<b>54</b>
3.5.1	Mathematical model to estimate the distance between sensors . . . . .	54
3.5.2	Constructive characteristics of the tactile system . . . . .	58
3.5.3	Temperature and force characterization . . . . .	60
3.5.4	Experimental validation . . . . .	61
<b>4</b>	<b>RESULTS AND DISCUSSION . . . . .</b>	<b>63</b>
<b>4.1</b>	<b>Instrumented claws's simulation and experimental results . . . . .</b>	<b>63</b>
4.1.1	FEM analysis . . . . .	63
4.1.2	Temperature characterization . . . . .	64
4.1.3	Strain characterization . . . . .	65
4.1.4	Compression tests . . . . .	68

4.1.5 Experimental validation . . . . . 71

**4.2 Tactile system’s experimental results . . . . . 73**

4.2.1 Temperature and force characterization . . . . . 73

4.2.2 Experimental validation . . . . . 76

**5 CONCLUSIONS AND FUTURE WORKS . . . . . 79**

**BIBLIOGRAPHY . . . . . 81**

# 1 Introduction

## 1.1 Motivation and justification

The three Industrial Revolutions took place between the 18th and 20th centuries and can be considered historic landmarks for humanity as they were the main consequence for the transition from a rural and feudal to an industrial and capitalist society (PRISECARU, 2016). During this period, due to the emergence of a set of technologies in the areas of mechanics, electrical and computing, it was possible to improve the manufacturing processes of the industries in terms of productivity, efficiency and quality of the products (ROMEO et al., 2020).

Result of the technological advances focused on continuous evolution, the so-called Industry 4.0 consists of the fourth stage of industrialization and represents what is most modern in terms of manufacturing processes today. This phase has as one of its main characteristics the use of intelligent devices, equipped with sensors, microprocessors and complete embedded systems that enable a real-time connection of physical and digital systems (BAHRIN et al., 2016) and enable a productive flow to be obtained fully optimized, integrated and automated (VAIDYA; AMBAD; BHOSLE, 2018). Among the new tools of this phase, additive manufacturing, the Internet of Things (IoT) and artificial intelligence are standout technologies (BAHRIN et al., 2016).

The introduction of robots into the industrial environment can be considered as a significant technological investment in the automation of manufacturing processes to achieve better results in the production chain. The consistency and precision associated with the result of the service performed by them can be understood as advantages when employing a robotic operator to complement the inabilities of a human worker (SHERWANI; ASAD; IBRAHIM, 2020).

Unlike Computer Integrated Manufacturing (CIM), in which the production process is completely controlled by computers and does not require human participation, the arrival of Industry 4.0 introduced a change in manipulators operation from an isolated performance from the human collaborator for a cooperative human-robot approach in many situations. This strategy guarantees an improvement of the use of resources and productivity by combining the characteristics of robots with the flexibility and dexterity of humans in dealing with unexpected and non-repetitive tasks. Thus, the work-space in industrial environments has been rethought in organizational terms in order to ensure the protection of human employees who interact with robots (THOBEN; WIESNER; WUEST, 2017).

The application of robots in the medical and healthcare fields is another case that involves direct interactions between humans and robots and it has become increasingly common to make medical procedures more reliable and safe (OKAMURA; MATARIĆ; CHRISTENSEN, 2010). Robotic systems enable more intense treatment, greater repeatability and reduce the therapists' workload when applied in rehabilitation processes (GASSERT; DIETZ, 2018). In terms of surgical procedures, many benefits were obtained with the participation of robots, as they compensate for the limitations of dexterity and precision of humans in the manipulation of micro-instruments. In addition, surgeon exposure to ionizing radiation and physical exhaustion during very long procedures can be reduced (OKAMURA, 2009). Finally, socially assistive robotics (SAR) is another robot-based strategy to motivate social and cognitive therapy through human-robot interaction (LANGER et al., 2019).

Despite performing many functions with mastery, robotic manipulators still have difficulties in executing some tasks that require high dexterity and precision such as heavy machining processes. In these situations, the unstable contact between tool and part associated with low rigidity of the robot joints may lead to deformations in the robot's joints and compromise the performance of its control system (PHAN et al., 2020). Therefore, algorithms that may compensate for these effects and offer better positioning accuracy can be implemented by monitoring the interaction forces and torques acting on the manipulator tool such as in machining processes (LI et al., 2019).

For the presented reasons, research involving more sensitive, accurate and reduced size sensors has become relevant to amplify the proprioception and tactile sensitivity of robots to improve their ability to perceive their own shape and detect external stimuli in an unstructured environment (SHE et al., 2020). Thus, it is possible to reach intelligent systems that can sense, interpret and react to stimuli quickly and efficiently (THOBEN; WIESNER; WUEST, 2017) and to ensure a safer working environment.

An important aspect of engineering projects is to design machines or robots that can carry out a series of activities without putting at risk the integrity of their mechanical structure. In order to achieve uninterrupted manufacturing processes with a low need for human direct intervention, some real-time monitoring techniques have been implemented in the industrial environment as a predictive maintenance strategy to improve useful life and efficiency of the equipment (CACHADA et al., 2018). In automated machining processes, the data obtained from sensors installed in work tools can provide the operators with useful information to guide the correct switch off the machine tool which affects the product quality and the production rate.

Strain rosettes are a common technique in which a set of strain sensors are used to evaluate the state of mechanical stress and strain during equipment operation. The configuration of strain rosette consists of a specific sensors arrangement that is placed over

a free surface of the system. With the strain data of the rosette, it is possible to determine the critical values of the stress-strain pair in the structure region in which the sensors are installed by applying the theory of elasticity. Thus, it is possible to evaluate if the project resistance limits are exceeded and if the components suffer the risk of failure (IRIARTE et al., 2021).

Chelladurai, Jain e Vyas (2008) has developed a monitoring system instrumented with a strain gauge bridge and two accelerometers to detect flank wear on a cutting tool during a machining process. The collected vibration and deformation data were used as input to an artificial neural network (ANN) and as output the network provides a prediction of the level of flank wear on the tool.

In the instrumentation market, optical fiber sensors have increasingly stood out as safety equipment for application in an industrial environment. This fact is due to its intrinsic characteristics such as compact size and chemical stability (PETERS, 2010). In addition, since the electrical and electronic components that makeup robots can interfere with the measurement results of electrically-based sensors (such as electric strain gauges), their electromagnetic immunity makes optical fiber sensors suitable for instrumenting this type of equipment (KERSEY et al., 1997). Additionally, the use of optical fiber sensors to instrument electromechanical and robotic equipment does not require an exquisite alignment with the monitored moving parts or an adaptation of the mechanical structure of the equipment for its installation differently from some other sensors such as encoders and potentiometers (LEAL-JUNIOR et al., 2018b).

Among the types of existing fiber sensors, the ones based on Fiber Bragg Grating (FBG) stand out for an application in industrial robotics due to their high sensitivity to deformation and their multiplexing capacity, which enables the inscription of several FBG sensors in a single fiber (QUANDT et al., 2015). Using multiplexed sensors certifies that a single optical fiber can be used as an optical signal transmission and reception channel in the measurement of different parameters. For this reason, it is possible to monitor in real-time sets of robotic devices that work cooperatively to perform a task using a reduced amount of cables. Applying such a strategy results in a reduction in costs and enables better use of the workspace (LEAL-JUNIOR et al., 2020b).

In the medical field, minimally invasive surgery (MIS) has some peculiarities such as instruments' long length and high stiffness that can affect the quality of the surgery results. These attributes end up limiting the reception of contact force information and reducing the tactile sensitivity of the medics (BANDARI; DARGAHI; PACKIRISAMY, 2019). Because of that, they lose their haptic perception and cannot have accurate control of hand movements (JASCHINSKI et al., 2018). Some research shows that the lack of contact force feedback causes an increase of about 50 percent in the average value and doubles the peak value of the force on human tissues (WAGNER; HOWE; STYLOPOULOS, 2002). In

the case of minimally invasive robotic surgery (MIRS), as the procedure is performed by robots, force feedback is eliminated. Recovering this sensitivity through tactile sensors has been an alternative found by some research groups. Song, Kim e Lee (2011) proposed a robotic manipulator with 7 DoF for MIS tests. The manipulator tool is instrumented with a sensor system based on FBGs to measure the interaction forces during surgery. The wavelength modulation sensing principle attached to Bragg wavelength shift provides to the FBGs independence of the optical source power fluctuations and immunity to connection losses.

Another important type of application of these sensors is the smart textiles, a wearable sensor technology that is commonly applied to monitoring physiological parameters and other aspects related to human health as kinematics and dynamics aspects of the human gait, body temperature, heart and respiration rate. This type of technology also plays an important role in quantifying interactions with the environment, such as detecting forces between users and objects (LEAL-JUNIOR et al., 2020a). Leal-Junior et al. (2018b) proposed a system using polymeric optical fiber (POF) sensors to monitor knee angles and human-robot interaction forces in a lower limb exoskeleton. In this type of application, monitoring these parameters is relevant when it comes to quantifying the quality of a human gait rehabilitation process.

This work aims to develop FBG-based tactile and end-effectors' structural integrity monitoring systems for robotic manipulators. A multiplexed system of sensors in a smart textile is installed in the robot body to detect stimuli and robot-environment and human-robot interactions during the execution of collaborative tasks. The processing of the response of the FBGs set to the stimuli allows estimating its intensity and the region of the robot body where the contact occurred. This guarantees the robot a greater capacity for proprioception and adaptation in unstructured environments to carry out its tasks efficiently. For the case of the robot end-effector, it is proposed that a set of strain gauges based on FBGs be positioned according to a strain rosette configuration in the robot claw, in order to estimate the critical stresses and strains in the region. This predictive maintenance technique can be implemented to ensure longer equipment life by evaluating whether the stress and strain limits established in the project are being exceeded during the robot operation.

## 1.2 Objectives

This master's thesis aims to develop FBG-based solutions for robotic manipulators that allow monitoring of the robot interactions with humans and with the environment and estimate the mechanical strains and stresses in the manipulator tool.

The specific objectives of this master's thesis are:

1. Development and practical implementation of an instrumented claw for robotic manipulators to estimate mechanical strains and stresses in the end effector during the robot operation.
2. Design and manufacture of FBG-based smart textiles to improve the tactile sensitivity of a robotic manipulator.
3. Installation and testing of the smart textiles to monitor the interaction with the environment, including interaction with humans, during the operation of a didactic robotic manipulator.
4. Experimental validation in the real environment of the sensor systems previously developed for the Kuka KR3 didactic robotic manipulator.

## 1.3 Contributions

One of the main contributions of this dissertation is the novelty of the application of FBG-based strain gauges in a strain rosette pattern to estimate the critical stress-strain pair in an instrumented claw. The estimation of the critical strain-stress pair is a useful strategy to check if an equipment structure is at risk of failure during service, however it is not a common approach in the literature for tools of robotic manipulators.

The other one is the development of a tactile system using optical fiber sensors to detect contact localization and the force during interactions with the environment. Optical fiber sensors are useful for robotic devices due to their immunity to electromagnetic noise which can come from the robot's components.

## 1.4 Publications

The work presented in this dissertation originated the following publications:

1. **Journal - V. Biazi**, C. A. F. Marques, A. Frizera-Neto and A. G. Leal-Junior, "FBG-embedded robotic manipulator tool for structural integrity monitoring from critical strain-stress pair estimation.", *IEEE Sensors Journal*, doi: 10.1109/JSEN.2022.3149459.

Others works were published about other topics and as a consequence of the interaction with the research group during the work development.

1. **Journal - V. Biazi**, L. Avellar, A. Frizera, A. Leal-Junior, "Influence of Two-Plane Position and Stress on Intensity-Variation-Based Sensors: Towards Shape Sensing in Polymer Optical Fibers.", *Sensors*, vol. 21, no. 23, p. 7848, doi: 10.3390/s21237848.

2. **Journal - Leal-Junior, A.; Avellar, L.; Biazi, V.; Soares, M. S.; Frizera, A.; Marques, C.**; "Multifunctional flexible optical waveguide sensor: on the bioinspiration for ultra-

sensitive sensors development.”, *Opto-Eletronic Advances*, 2021, doi: 10.29026/oea.2022.210098.

3. **Book Chapter** - Leal-Junior, A. G.; Frizera-Neto, A.; **Biazi, V.**; Marques, C.; “Optical fiber sensors applications for human health.” in *Optical Fiber Sensors for the Next Generation of Rehabilitation Robotics.*, Elsevier, 2022, doi: 10.1016/B978-0-32-385952-3.00023-8.

## 1.5 Dissertation Structure

This document is divided into five chapters introduced as follows.

Chapter 1 presents the motivations and the problem to be solved. The justification, relevant works related to the theme, and main goals of the dissertation are also presented.

Chapter 2 presents the theoretical background used as a basis for the development of the work. The definition and characteristics of robotic manipulators, stress and strain transformation equations, the operating principles of optical fiber, and the basics of FBG sensors are presented in this chapter.

Chapter 3 presents the materials and methods used during the research. It presents the manufacturing setup of the sensors, the design of the proposed systems, and also the experimental setups for characterization of the FBGs. Parameters of a static FEM simulation to qualitatively characterize claws sensors are also presented in this chapter. Finally, the experiments for validation of the systems are also presented in the end of the chapter.

Chapter 4 presents the main results obtained in the research and the discussion about them. In this chapter, there are the results and analysis of the FEM simulation as well as the characterization and some sensors relevant parameters for both sensor systems. The results of the validation experiments are presented as well as some relevant information obtained from them.

Chapter 5 presents the conclusions of the research and some suggestions of future works.



## 2 Theoretical Background

In this chapter, relevant concepts about robotic manipulators and optical fiber-based sensors are presented, with emphasis on FBGs and some of their applications. The transformation equations to obtain critical stresses and strains for elastic materials and their importance for structural health monitoring are also presented.

### 2.1 Robotic Manipulators

A robotic manipulator can be defined as equipment formed by a set of mechanical, electrical and electronic components that is programmed to perform repetitive tasks automatically (CRAIG, 2009). They are formed by links coupled through joints that allow relative movement between their rigid bodies. The robot actuators connected to the joints are responsible for animating the robot's mechanical parts. The sensory system of robots is formed by proprioceptive sensors which acquire data from the internal components and exteroceptive sensors which acquire the external status of the environment. The control system of a robot is the part responsible to provide commands to the actuators based on the goals of a task to be performed and the feedbacked information of the sensors. A manipulator can be defined in terms of its fundamental structure as an open kinematic chain or closed kinematic chain manipulator. An open kinematic chain manipulator was a sequence of links connecting its base to the end effector whereas a closed kinematic chain manipulator was a group of links connected as a loop (SICILIANO et al., 2010). Figure 1 presents examples of open and closed kinematic chain manipulators, respectively.

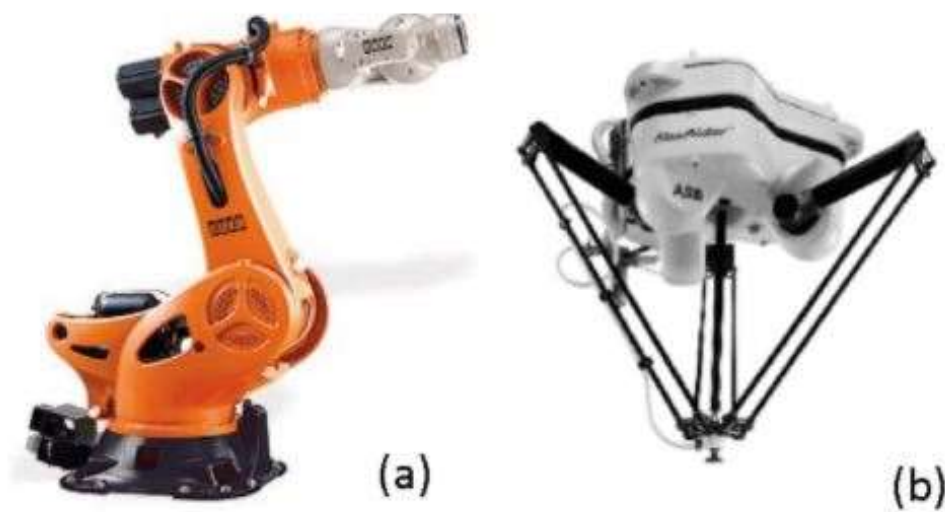


Figure 1 – Manipulators with (a) open kinematic chain and (b) closed kinematic chain. (SICILIANO et al., 2010)

Moreover, the manipulators are mechanisms used to move objects spatially and for this reason, a spatial description of the position and orientation of bodies in space is commonly employed for studies involving industrial robotics. Frames of reference are attached to objects and then their position and orientation are described in terms of another frame of reference. Whereas any frame of reference can be used to express spatial coordinates, it is important to know the coordinate transformations that lead one frame to another (CRAIG, 2009).

If 1 and 2 are coordinate systems with distinct position and orientation, the homogeneous transformation matrix  $T$  takes a vector described in frame 1 to a vector in frame 2 applying a set of translations and rotations. Eq. 2.1 shows this transformation described mathematically.

$$P^2 = {}^2_1 T \cdot P^1, \quad (2.1)$$

where  $P^2$  is the vector on the reference frame 2,  $P^1$  is the vector on the reference frame 1 and  ${}^2_1 T$  is the transformation matrix from reference frame 2 to reference frame 1.

The forward kinematics of a robotic manipulator corresponds to a set of mathematical equations that allow representing the position and orientation of the robot's end-effector as a function of its joint angles in a base reference system (SICILIANO et al., 2010). For a manipulator with  $n$  joints, it is possible to obtain the transformation matrix from the tool's reference system to the manipulator base's reference system through the multiplication of transformation matrices between adjacent joints (CRAIG, 2009). Eq. 2.2 and 2.3 allow obtaining the position of the robot tool in the base reference system as long as the transformation matrices are known.

$$P^B = {}^B_1 T \cdot {}^1_2 T \cdot \dots \cdot {}^{n-1}_n T \cdot {}^n_T T \cdot P^T, \quad (2.2)$$

$$P^B = {}^B_T T \cdot P^T, \quad (2.3)$$

where  $P^B$  is the vector on the base reference frame,  $P^T$  is the vector on the tool reference frame and  ${}^n_{n-1} T$  is the transformation matrix from reference frame  $n$  to reference frame  $n - 1$  and  ${}^B_T T$  is the transformation matrix from the tool reference frame to base reference frame.

There is a set of non-linear geometric equations called inverse kinematics of the manipulator that make it possible to determine the joint angles that bring the tool to the desired pose as shown in Figure 2(a).

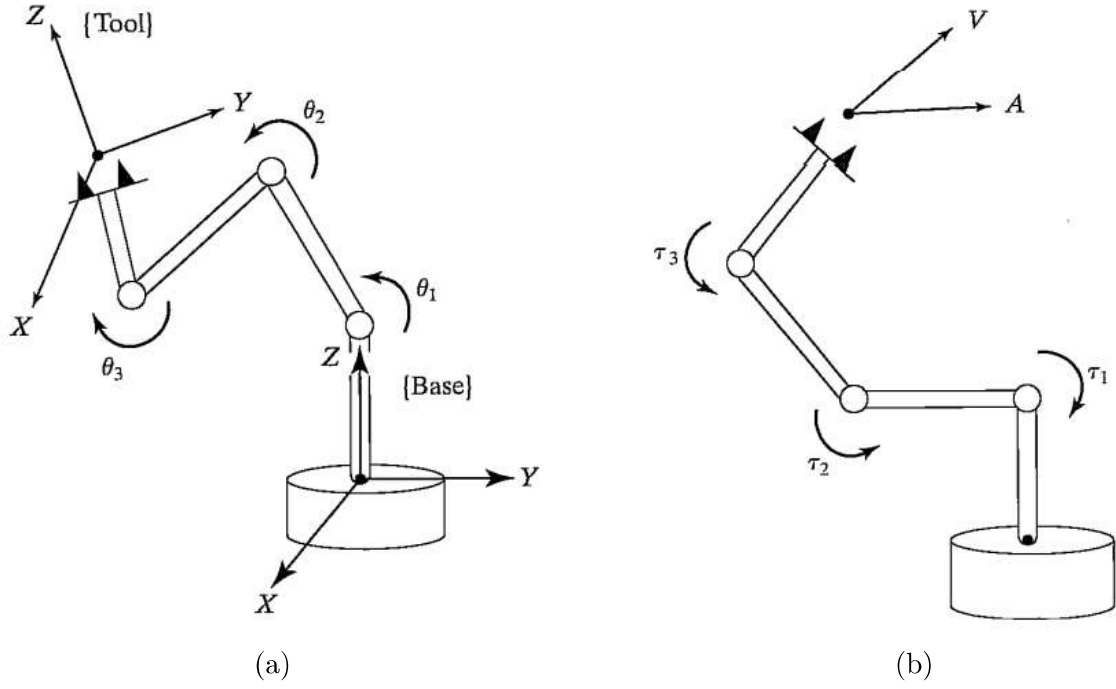


Figure 2 – Representation of a manipulator (a) inverse kinematics and (b) dynamics (CRAIG, 2009).

Eq. 2.4 describes in general form the inverse kinematics of a manipulator.

$$\theta_i(t) = f(x(t), y(t), z(t)), \quad (2.4)$$

where  $\theta_i(t)$  is the angle relative to joint  $i$ , and  $x(t)$ ,  $y(t)$  and  $z(t)$  are the positions of the end effector in the coordinates  $x$ ,  $y$  and  $z$  of the base reference frame.

To move the robotic manipulator, it is necessary to apply a set of torques to its joints that are dependent on the desired spatial path, velocities and accelerations and, in addition, to the mass properties of the manipulator. This approach is important in the simulation, design and conception of control algorithms since it takes into account part of the robot's mechanical characteristics and guarantees proximity to the real physical system (SPONG et al., 2006).

The inverse dynamics of a manipulator (Figure 2(b)) consists in determining the joint torques necessary to generate a trajectory with specific joint angles, velocities and accelerations once the forces acting on the end effector are known. Eq. 2.5 is a representation of the inverse dynamics equations for a generic manipulator.

$$\tau_i(t) = f(\ddot{\theta}_1(t), \dots, \ddot{\theta}_n(t), \dot{\theta}_1(t), \dots, \dot{\theta}_n(t), \theta_1(t), \dots, \theta_n(t), h_e(t)), \quad (2.5)$$

where  $\tau_i$  is the torque on the joint  $i$ ,  $\ddot{\theta}_i$  is the angular acceleration of joint  $n$ ,  $\dot{\theta}_i$  is the angular velocity of the joint  $n$  and  $h_e$  is the forces and torques on the manipulator

body.

Industrial robots' common characteristics such as adaptability, flexibility, ample working space and relatively low cost make them promising for application in many industrial processes (SCHNEIDER et al., 2014). Initially, their participation in the manufacturing environment consisted of performing functions that could put the integrity of human employees at risk, such as the transport of heavy loads (SHERWANI; ASAD; IBRAHIM, 2020) or functions that required a high degree of repeatability such as moving objects, painting and welding (DUMAS et al., 2012).

The cyber-physical connection which comes from Industry 4.0 drove the emergence of smart grids which served as a basis for the appearance of the concept of collaborative robots. This type of robot has been included in the minimally invasive surgery (MIS) scenario. They are characterized by having many modern sensors and control strategies that compensate for the limitations of human dexterity and precision in handling instruments of MIS, for example, (OKAMURA, 2009). In addition, the surgeon's exposure to ionizing radiation and physical exhaustion during very long procedures can be reduced when they work with cobots (SCHOSTEK; SCHURR; BUESS, 2009).

## 2.2 Strain gauges and strain rosettes

Strain gauges are sensors normally applied to measure parameters such as deformation, pressure, force and others. Their operation principle is related to the electrical resistance variation of their fine metal wire that occurs when they are on an object surface that is tensioned or compressed. The strain gauge's sensitivity defines how it behaves in relation to uniaxial stress applied in the direction of the strain gauge longitudinal axis. For the metal strain gauge (Eq. 2.6), the sensitivity or gauge factor ( $S$ ) is the ratio between the change of resistance ( $\frac{\Delta R}{R}$ ) and the applied strain on the gauge axis ( $\epsilon$ ) (KUMAR et al., 2012). Strain gauge sensitivity can be defined only when there is no strain applied in the direction perpendicular to the gauge axis.

$$S = \frac{\frac{\Delta R}{R}}{\epsilon}. \quad (2.6)$$

A group of three strain gauges may be positioned in a specific pattern, known as strain rosette, to monitor the principal strains and stresses on a point of an equipment surface in service. There are many types of strain rosette settings and these different arrangements result in distinct transformation equations, based on elasticity theory and materials mechanical properties. The chosen pattern needs to meet geometric and dimensional restrictions on the body of the monitored component, and it must be able to detect the strains on the analysis region. Some of the most common configurations are the Y,

delta and rectangular arrangement as shown in Figure 3 (ROSSETTO; BRAY; LEVI, 1975).

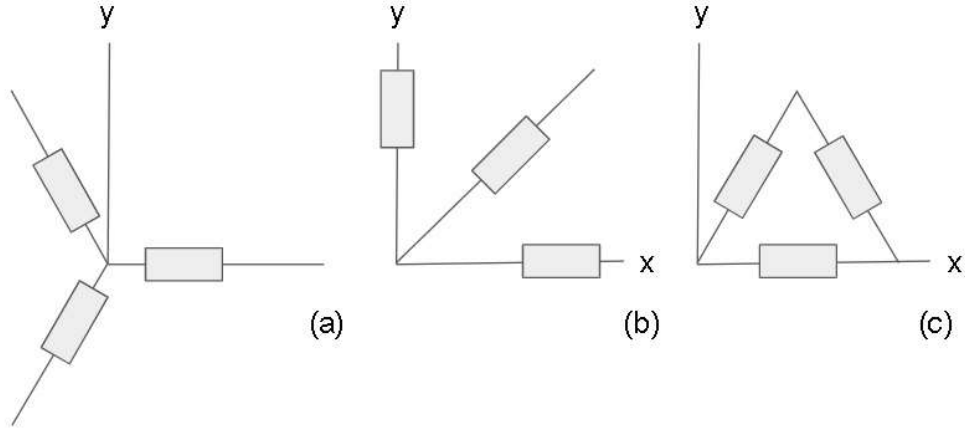


Figure 3 – Some of the strain rosette configurations: (a) Y, (b) rectangular and (c) delta.

In the Y configuration, the gauges are positioned with a  $120^\circ$  angle to each other. Moreover, there are other types of Y in which the angles between the gauges are different from  $120^\circ$ . In the rectangular rosette, two sensors are placed with a  $90^\circ$  angle between them and a third with a generic angle in relation to the others. The sensors are placed over the edges of a triangle in the delta configuration (ROSSETTO; BRAY; LEVI, 1975).

It is necessary to define a Cartesian coordinate frame to be utilized as a reference to the extensometers and this is a relevant step to get the principal plane stains on a body surface. The generic strain transformation equations (Eq. 2.7-2.9) from (BEER et al., 2017) may be used to get the normal strain on the x and y axes and the shear strain on the xy-plane.

$$\epsilon_a = \epsilon_x \cdot \cos^2\theta_a + \epsilon_y \cdot \sin^2\theta_a + \gamma_{xy} \cdot \sin\theta_a \cdot \cos\theta_a, \quad (2.7)$$

$$\epsilon_b = \epsilon_x \cdot \cos^2\theta_b + \epsilon_y \cdot \sin^2\theta_b + \gamma_{xy} \cdot \sin\theta_b \cdot \cos\theta_b, \quad (2.8)$$

$$\epsilon_c = \epsilon_x \cdot \cos^2\theta_c + \epsilon_y \cdot \sin^2\theta_c + \gamma_{xy} \cdot \sin\theta_c \cdot \cos\theta_c. \quad (2.9)$$

$\epsilon_a$ ,  $\epsilon_b$  and  $\epsilon_c$  are the normal strain on the three rosette sensors,  $\theta_a$ ,  $\theta_b$  and  $\theta_c$  are the angle between sensors axis and x-axis,  $\epsilon_x$  is the normal strain on x-axis,  $\epsilon_y$  is the normal strain on y-axis and  $\gamma_{xy}$  is the shear strain on the xy-plane. Solving the three equations simultaneously, it is possible to determine  $\epsilon_x$ ,  $\epsilon_y$  and  $\gamma_{xy}$ .

The maximum and minimum normal strains that may be found on a plane surface are named principal strains and they have no shear strain associated with them in the strain

element. The maximum shear strain on a plane is another important variable in resistance analysis and it is associated with average normal strains on the strain element. These parameters are the most important to evaluate if the body will maintain its structural integrity at service. Figure 4 shows the representation of the variables on a plane strain element.

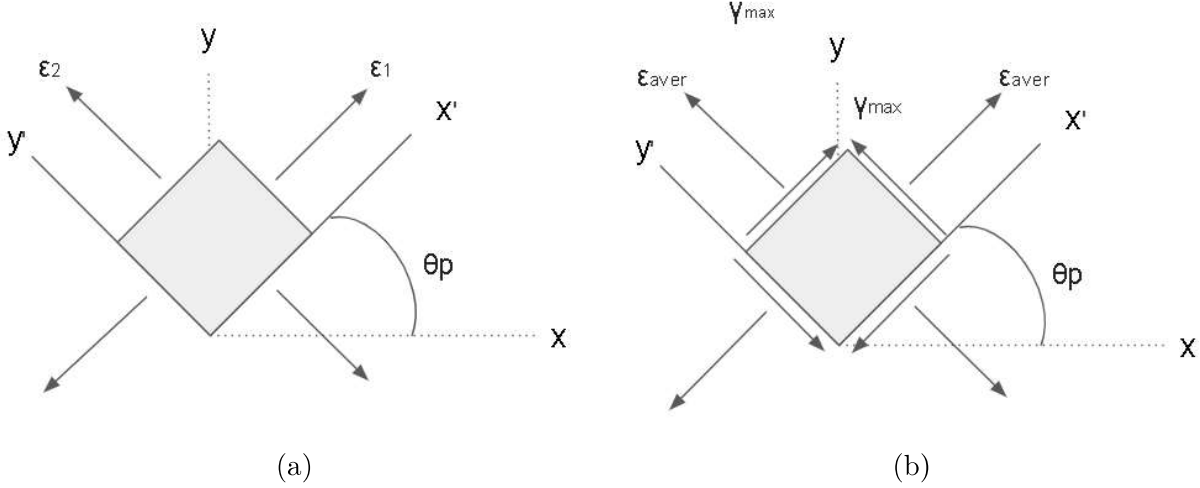


Figure 4 – Strain elements oriented to (a) principal strains and (b) maximum shear strain.

The principal strains values ( $\epsilon_{1,2}$ ) and the orientation angle of the principal strains to  $x$ -axis ( $\theta_p$ ) may be obtained using  $\epsilon_x$ ,  $\epsilon_y$  and  $\gamma_{xy}$  and applying Eq. 2.10 and 2.11. The equations used for the strains and stresses analysis are from Beer et al. (2017).

$$\epsilon_{1,2} = \frac{\epsilon_x + \epsilon_y}{2} \pm \sqrt{\left(\frac{\epsilon_x - \epsilon_y}{2}\right)^2 + \left(\frac{\gamma_{xy}}{2}\right)^2}, \quad (2.10)$$

$$\tan(2 \cdot \theta_p) = \frac{\gamma_{xy}}{\epsilon_x - \epsilon_y}. \quad (2.11)$$

The maximum shear strain ( $\gamma_{max}$ ), average normal strain ( $\epsilon_{aver}$ ) and their orientation angle relative to  $x$ -axis ( $\theta_s$ ) may be obtained using  $\epsilon_x$ ,  $\epsilon_y$  and  $\gamma_{xy}$  on Eq. 2.12-2.14.

$$\gamma_{max} = \sqrt{\left(\frac{\epsilon_x - \epsilon_y}{2}\right)^2 + \left(\frac{\gamma_{xy}}{2}\right)^2}, \quad (2.12)$$

$$\epsilon_{aver} = \frac{\epsilon_x + \epsilon_y}{2}, \quad (2.13)$$

$$\tan(2 \cdot \theta_s) = -\left(\frac{\epsilon_x - \epsilon_y}{\gamma_{xy}}\right). \quad (2.14)$$

Assuming that the structural material is homogeneous throughout its body, has a linear elastic behavior and has the same properties in all directions (isotropic), a stress

analysis may also be made. Normal stress actuating in any direction may induce strains perpendicularly to it and they can be related by material Young's modulus and Poisson's ratio. Computing the stresses effects on the perpendicular axis, Hooke's law can be written such as Eq. 2.15-2.17.

$$\epsilon_x = \frac{1}{E} \cdot [\sigma_x - \nu \cdot (\sigma_y + \sigma_z)], \quad (2.15)$$

$$\epsilon_y = \frac{1}{E} \cdot [\sigma_y - \nu \cdot (\sigma_x + \sigma_z)], \quad (2.16)$$

$$\epsilon_z = \frac{1}{E} \cdot [\sigma_z - \nu \cdot (\sigma_x + \sigma_y)], \quad (2.17)$$

where  $\sigma_x$  is the normal stress on the x-axis,  $\sigma_y$  is the normal stress on the y-axis,  $\sigma_z$  is the normal stress on the z-axis,  $E$  is the material Young's modulus and  $\nu$  is the material Poisson's ratio. When a surface of a rigid body, in which there is no existence of load, is free of stress and the points in this surface are under a plane stress state. Assuming that  $\sigma_z=0$ , Eq. 2.15-2.17 may be rearranged such as Eq. 2.19-2.20 to get  $\sigma_x$ ,  $\sigma_y$  and  $\epsilon_z$ .

$$\sigma_x = \frac{E \cdot \epsilon_x + \nu \cdot E \cdot \epsilon_y}{1 - \nu^2}, \quad (2.18)$$

$$\sigma_y = \frac{E \cdot \epsilon_y + \nu \cdot E \cdot \epsilon_x}{1 - \nu^2}, \quad (2.19)$$

$$\epsilon_z = -\frac{\nu \cdot (\epsilon_x + \epsilon_y)}{1 - \nu}. \quad (2.20)$$

The shear stresses, differently from the normal ones, only have effects over shear strain in its own plane. They are linearly related by the shear modulus of the material (Eq. 2.21).

$$\tau_{xy} = G \cdot \gamma_{xy}, \quad (2.21)$$

where  $\tau_{xy}$  is the shear stress on the xy-plane and  $G$  is the shear modulus of the material. An important point of this analysis is that normal stresses do not affect the shear strains. The shear modulus of the material is directly related to Young's modulus and Poisson's ratio of the material as presented in Eq. 2.22.

$$G = \frac{E}{2 \cdot (1 + \nu)}. \quad (2.22)$$

It is known that the stress state is related to the strain state by material mechanical properties. An analogy to Eq. 2.10 and 2.11 for stresses gives the principal stresses ( $\sigma_{1,2}$ ) and the orientation angle ( $\theta_{ps}$ ) of the principal stresses relative to x-axis (Eq. 2.23 and 2.24).

$$\sigma_{1,2} = \frac{\sigma_x + \sigma_y}{2} \pm \sqrt{\left(\frac{\sigma_x - \sigma_y}{2}\right)^2 + \tau_{xy}^2}, \quad (2.23)$$

$$\tan(2 \cdot \theta_{ps}) = \frac{\tau_{xy}}{\frac{\sigma_x - \sigma_y}{2}}. \quad (2.24)$$

Maximum shear stress, average normal stress, and their orientation angle relative to x-axis may be obtained using  $\sigma_x$ ,  $\sigma_y$  and  $\tau_{xy}$  on Eq. 2.25-2.27.

$$\tau_{max} = \sqrt{\left(\frac{\sigma_x - \sigma_y}{2}\right)^2 + \tau_{xy}^2}, \quad (2.25)$$

$$\sigma_{aver} = \frac{\sigma_x + \sigma_y}{2}, \quad (2.26)$$

$$\tan(2 \cdot \theta_{ss}) = -\frac{\frac{\sigma_x - \sigma_y}{2}}{\tau_{xy}}. \quad (2.27)$$

Figure 5 presents the configurations over the Cartesian coordinate frame and the respective angles related to each sensor on the rosette configuration presented previously.

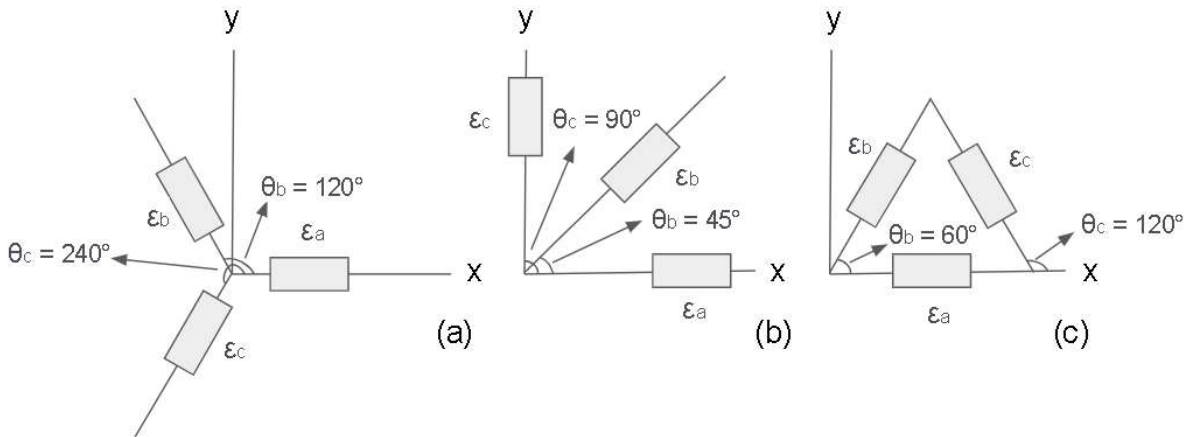


Figure 5 – Strain rosette parameters for (a) Y, (b) rectangular and (c) delta configurations.

By selecting the angles that define a specific rosette structure, it is possible to relate the response of the sensors with the desired critical strains and stresses. Independent of the rosette pattern chosen for the analysis, the principal strains and stresses are the



same for all configurations. For the Y rosette, the angles values for this case are  $\theta_a=0^\circ$ ,  $\theta_b=120^\circ$  and  $\theta_c=240^\circ$ . By substituting the angles values on Eq. 2.7-2.9, the equations are reduced to Eq. 2.28-2.30 and the strains  $\epsilon_x$ ,  $\epsilon_y$  and  $\gamma_{xy}$  may be obtained for Y rosette data.

$$\epsilon_x = \epsilon_a, \quad (2.28)$$

$$\epsilon_y = \frac{1}{3} \cdot (2 \cdot \epsilon_b + 2 \cdot \epsilon_c - \epsilon_a), \quad (2.29)$$

$$\gamma_{xy} = \frac{2}{\sqrt{3}} \cdot (\epsilon_c - \epsilon_b). \quad (2.30)$$

For the rectangular rosette, the angles values for this case are  $\theta_a=0^\circ$ ,  $\theta_b=45^\circ$  and  $\theta_c=90^\circ$  and the strain values are obtained from Eq. 2.31-2.33.

$$\epsilon_x = \epsilon_a, \quad (2.31)$$

$$\epsilon_y = \epsilon_c, \quad (2.32)$$

$$\gamma_{xy} = 2 \cdot \epsilon_b - \epsilon_a - \epsilon_c. \quad (2.33)$$

The same process can be repeated to delta arrangement, by substituting the angles values of  $\theta_a=0^\circ$ ,  $\theta_b=60^\circ$  and  $\theta_c=120^\circ$ , the equations are reduced to Eq. 2.34-2.36.

$$\epsilon_x = \epsilon_a, \quad (2.34)$$

$$\epsilon_y = \frac{1}{3} \cdot (2 \cdot \epsilon_b + 2 \cdot \epsilon_c - \epsilon_a), \quad (2.35)$$

$$\gamma_{xy} = \frac{2}{\sqrt{3}} \cdot (\epsilon_b - \epsilon_c). \quad (2.36)$$

## 2.3 Optical Fiber Overview

Optical fiber can be defined as a waveguide to transport light between two different locations in space. Light propagation through an optical fiber, under the point-of-view of geometric optics, by successive reflections along its length is possible due to the core's higher refractive index than cladding. The fiber core and cladding are commonly surrounded by a jacket that provides robustness and mechanical protection (ADDANKI; AMIRI;

YUPAPIN, 2018).

When the light inside the fiber core meets the core-cladding interface at an angle greater than the so-called critical angle, then it undergoes a total internal reflection and propagates along the core length. By the Snell law, the critical angle is the incident angle of the light when the transmitted angle is  $90^\circ$  and can be obtained from Eq. 2.37.  $\theta_{crit}$  is the incident critical angle,  $n_{core}$  is the refractive index of the core and  $n_{clad}$  is the refractive index of the cladding.

$$\theta_{crit} = \arcsin\left(\frac{n_{core}}{n_{clad}}\right). \quad (2.37)$$

For a light beam coming from the external environment to couple an optical fiber, it must enter the fiber with an angle smaller than the acceptance angle. The sine of the acceptance angle defines the numerical aperture of an optical fiber (Eq. 2.38) and describes the amount of incoming light on the optical fiber core (ZIEMANN et al., 2008).  $NA$  is the numerical aperture of an optical fiber,  $\theta_{accep}$  is the acceptance angle and  $n_{ext}$  is the external refractive index.

$$NA = \sin(\theta_{accep}) = \sin(\theta_{crit}) \cdot \frac{n_{core}}{n_{ext}}. \quad (2.38)$$

Figure 6 shows a schematic of the conditions that must be met for the injection of light into the optical fiber ( $\theta < \theta_{accep}$ ) and for total internal reflection inside the optical fiber core ( $\alpha > \theta_{crit}$ ).

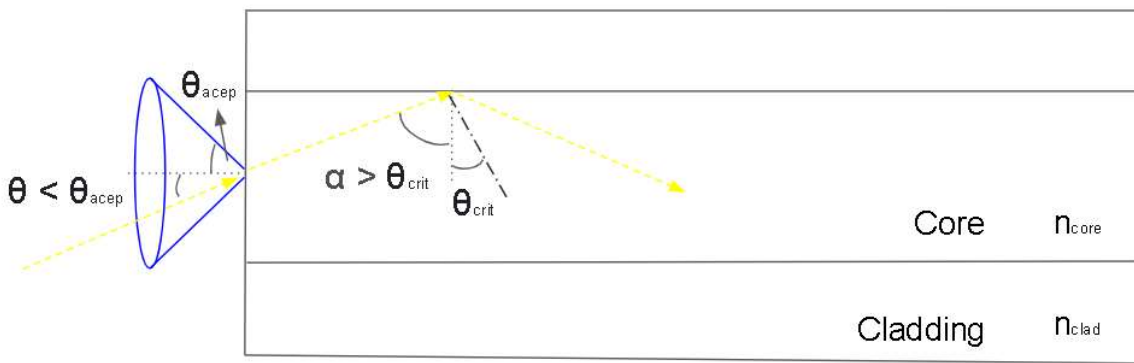


Figure 6 – Scheme of the light propagation on the optical fiber.

Technological advances in the late 20th century made it possible to manufacture new types of optical sources, amplification systems and modulation techniques that made the optical fibers a revolutionary tool for telecommunication systems (DIAZ et al., 2019). Besides their traditional use on telecommunication systems, optical fibers have become a consolidated technology for a series of sensing applications such as healthcare monitoring

(YU et al., 2019), environmental changes detection in industries (JOE et al., 2018), and structural and spacecraft health monitoring (BARRIAS et al., 2018; ECKE et al., 2001). One of the main reasons for them being widely used in the sensing field is their intrinsic characteristics such as low weight, compactness and chemical stability. Additionally, they are immune to electromagnetic fields which can appear when the electrical actuators are activated and distort the results from the conventional electronic-based sensors (PETERS, 2010). This technology has a substantial growth due to its characteristics and the diversity of parameters that can be monitored such as temperature, force, acceleration, liquid level, humidity, pressure, among others (LEAL-JUNIOR et al., 2018).

The optical fiber sensors operate in the modulation of the light guided by the optical fiber and may be based on intensity variation, phase modulation and wavelength encoding. In intensity variation sensors, there is a variation of optical power at the fiber output when the fiber is under the effect of the external parameter of interest. For this reason, variations in light source power can alter the sensor response leading to measurement errors. Nevertheless, their main advantages are their low price and high portability since they use simple and compact electronic components. This type of sensor is an efficient and easier to implement alternative when techniques to compensate for its sensitivity to light source deviations are used (LEAL-JUNIOR et al., 2018a).

In the modulated phase, light passes through an interferometer and is split into two beams. When one of the beams traverses the monitored environment it suffers a phase shift. The measurement is obtained by comparing the phase-shifted beam with the other beam which is isolated from the environment (JAIN; KALER, 2018).

The ones based on wavelength encoding, such as Fiber Bragg Grating (FBG), are important for high precision applications since their response is immune to light source power variations. The multiplexing capability of the FBG sensors is a differential characteristic to situations in which it is necessary to measure more than one parameter and to monitor a parameter at multiple points on a body (LING et al., 2007). Nevertheless, a conventional optical spectrum analyzer for interrogation these sensors are expensive, heavy and require a large workspace (WERNECK et al., 2013) making them difficult to use in portable applications such as real-time patient health monitoring. Research has been developed to obtain multiplexed intensity variation-based sensors which are less expensive and an easier to manufacture alternative such as done by (LEAL-JUNIOR et al., 2019).

## 2.4 Fiber Bragg Grating

FBG may be defined as a periodic variation that occurs on the refractive index of the optical fiber when it is exposed to an spatially periodic optical interference pattern (HILL; MELTZ, 1997). Figure 7 shows an optical fiber region with a FBG inscribed on its

core. The distance between successive peaks in the grating refractive index is called the grating period. The FBG works as a wavelength selective mirror by reflecting the optical signal transmitted through that fiber in a narrow spectral region centered on a specific wavelength named Bragg wavelength (HILL et al., 1978). Consequently, the reflection spectrum has an amplitude peak on the same spectral band (GE et al., 2014).

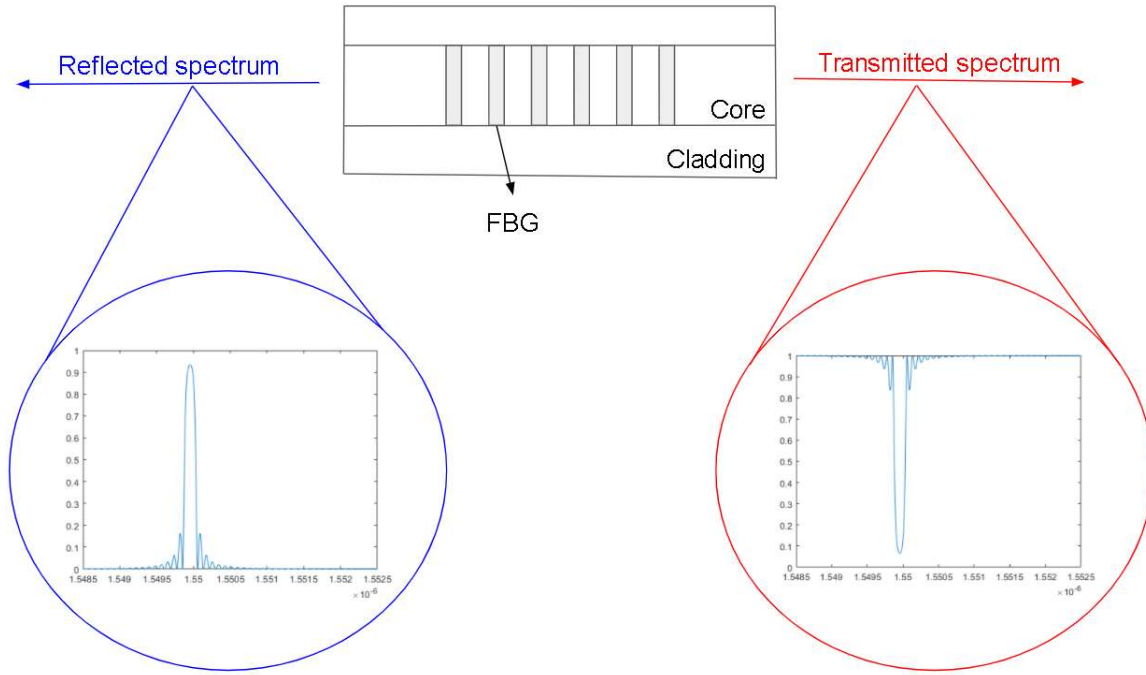


Figure 7 – Scheme of the FBG working principle.

To manufacture these sensors, a region of the optical fiber is exposed to an incident light beam with periodic spatial variation in intensity and, as a result, there is a change, also periodic, in the refractive index of the fiber core at the location reached by the light (LUO et al., 2017). Among the methods of manufacturing FBGs in fibers, one can mention the irradiation of an ultraviolet (UV) laser guided by a phase mask on the fiber (MARQUES et al., 2018) or the direct inscription with a femtosecond laser (LACRAZ et al., 2015).

This type of optical fiber sensor has intrinsic characteristics such as multiplexing capability which allows more than one of them to be inscribed on the same fiber reducing the necessity of a high number of optical channels and complex wiring (BETZ et al., 2006), and the wavelength-encoded data which reduces the errors related to optical power deviations on the optical source and to light noises (DIAZ et al., 2019). It is necessary to apply different configurations on the manufacturing equipment in order to produce FBGs with distinct design wavelengths ensuring that the information regarding the measures does not overlap and that the expected results are not masked (LEAL-JUNIOR et al., 2018). The Bragg wavelength can be defined as a function of the fiber core's effective

refractive index and grating period as shown in Eq. 2.39 (XIONG et al., 2018).

$$\lambda_B = 2 \cdot n_{eff} \cdot \Lambda, \quad (2.39)$$

where  $\lambda_B$  is the Bragg wavelength,  $n_{eff}$  is the fiber effective refractive index and  $\Lambda$  is the grating period. When the FBG suffers an axial elongation or a thermal expansion, there is a linear increase in the FBG period (HILL; MELTZ, 1997). Moreover, the effective refractive index may be affected by temperature and strain due to thermo-optic and photo-elastic effects, respectively. For this reason, a Bragg wavelength shift happens when the FBG is under the effect of a mechanical strain or temperature variation and FBGs can be used as a sensor to monitor such parameters. Eq. 2.40 presents how axial strain and temperature variation affect the Bragg wavelength position (HILL; MELTZ, 1997).

$$\lambda_B = \lambda_o \cdot [1 + (1 - P_e) \cdot \epsilon_{fiber} + (\alpha + \zeta) \cdot \Delta T], \quad (2.40)$$

where  $\lambda_o$  is the design Bragg wavelength,  $P_e$  is the fiber photo-elastic constant,  $\epsilon_{fiber}$  is the axial normal strain on the fiber,  $\alpha$  is the fiber thermal expansion coefficient,  $\zeta$  is the thermo-optic coefficient and  $\Delta T$  is the temperature variation.

If the FBG is embedded in a specific material, it is necessary to carry out an experimental characterization process between the central wavelength shift and the parameter of interest whereas characteristics of the coating material affect the sensor's behavior. The thermal expansion of the embedding material causes a change in the period of the FBG (MAGNE et al., 1997).

As temperature variations shift the Bragg wavelength in the reflection spectrum, they need to be compensated to avoid interference in the strain measurements. One approach to compensating for the effect of temperature is to add an extra FBG in a strain-free region of the structure. It is assumed that the strain does not interfere with the wavelength shift of the temperature compensation sensor. It is possible to extend the approach used by Díaz et al. (2017) to compensate for the effects of temperature variation on the response of strain sensors for different situations. The effects of temperature on the Bragg Wavelength is decoupled from the strain in Eq. (2.41). Each FBG is sensible to temperature and to the longitudinal strain.

$$\begin{bmatrix} \epsilon_1 \\ \epsilon_2 \\ \epsilon_3 \\ \Delta T \end{bmatrix} = \begin{bmatrix} k_{1,\epsilon} & 0 & 0 & k_{1,T} \\ 0 & k_{2,\epsilon} & 0 & k_{2,T} \\ 0 & 0 & k_{3,\epsilon} & k_{3,T} \\ 0 & 0 & 0 & k_{t,T} \end{bmatrix}^{-1} \cdot \begin{bmatrix} \Delta\lambda_{B,1} \\ \Delta\lambda_{B,2} \\ \Delta\lambda_{B,3} \\ \Delta\lambda_{B,t} \end{bmatrix}, \quad (2.41)$$

$k_{1,\epsilon}$ ,  $k_{2,\epsilon}$  and  $k_{3,\epsilon}$  are the strain sensitivities on the FBGs 1 to 3.  $k_{1,T}$ ,  $k_{2,T}$ ,  $k_{3,T}$

and  $k_{t,T}$  are the temperature variation sensitivities on the FBGs 1 to 3 and on the temperature compensation FBG.  $\epsilon_1$ ,  $\epsilon_2$  and  $\epsilon_3$  are the longitudinal strains on the FBGs 1 to 3.  $\Delta\lambda_{B,1}$ ,  $\Delta\lambda_{B,2}$ ,  $\Delta\lambda_{B,3}$  and  $\Delta\lambda_{B,t}$  are the wavelength shift on the FBGs 1 to 3 and on the temperature compensation FBG.  $\Delta T$  is the temperature variation on the claw.

The consolidated commercial FBG sensors use silica optical fibers as waveguides, however, polymeric optical fibers (POFs) have many characteristics intrinsic to their material to be a useful commercial solution. The POFs sensors have high strain limits and fracture toughness which provide adequate mechanical robustness for large strain measurements. Their lower Young's modulus compared with silica optical fiber results in more flexible sensors with higher dynamic range and sensitivity (LEAL-JUNIOR; FRIZERA; PONTES, 2018). Nevertheless, some problems are faced using POFs to implement the FBG-based sensor technology. The viscoelastic characteristics of polymers such as creep and relaxation can result in the hysteresis effect which is a difference between the sensor response when they are under cyclic conditions of loading (LEAL-JUNIOR et al., 2018c). Furthermore, the polymeric optical fiber Bragg gratings (POFBGs) face some difficulties with the interrogation process due to their relatively high losses ( $1 \text{ dB} \cdot \text{cm}^{-1}$ ) in the 1500nm region which is the spectral band in which most interrogation equipment operates. The unavailability of a single-mode coupler or the pigtailed source for POFs makes it necessary to connect them to silica fibers to be possible to monitor its reflection spectrum (WEBB, 2015). Since there is no equivalent splicer for POFs, the fibers have to be glued or connectorized. Most of these connections such as butt coupling are neither robust nor demountable and they cause losses on the reflected signal which results in an inappropriate Bragg response for sensing applications (ABANG; WEBB, 2012).

The description of the robotic manipulators, the operating principle of the optical fibers and their applications as sensors, the characteristics of FBGs, and the stress and strain transformation equations using elasticity theory presented in this chapter were used as basis for the manufacturing and testing of the systems shown in the next chapters.

## 3 Material and Methods

This chapter shows the materials and the techniques used in the development of the sensor systems. The system and equipment's in which the sensors were tested, the experimental setup for the sensors' manufacturing, the constructive characteristics of the sensor systems as well as the tests for validation of the systems after manufacturing are presented and detailed.

### 3.1 Briefly introduction of the sensors systems

The instrumented claws to be connected to the electric gripper are proposed with sensors installed on them to monitor its structural integrity during robot operation. The FBGs are positioned in a delta rosette pattern on the surface of the claws. The tactile system is composed of a group of smart textiles installed on the robot's links and each textile is equipped with several sensors so that it is able to detect interactions with the environment at all possible points. The FBGs were chosen as a solution in terms of sensors due to their multiplexing capability that allows the installation of many sensors using only one channel for optical fiber. Figure 8 presents the instrumented claws and the smart textiles installed on the robot's body, respectively.

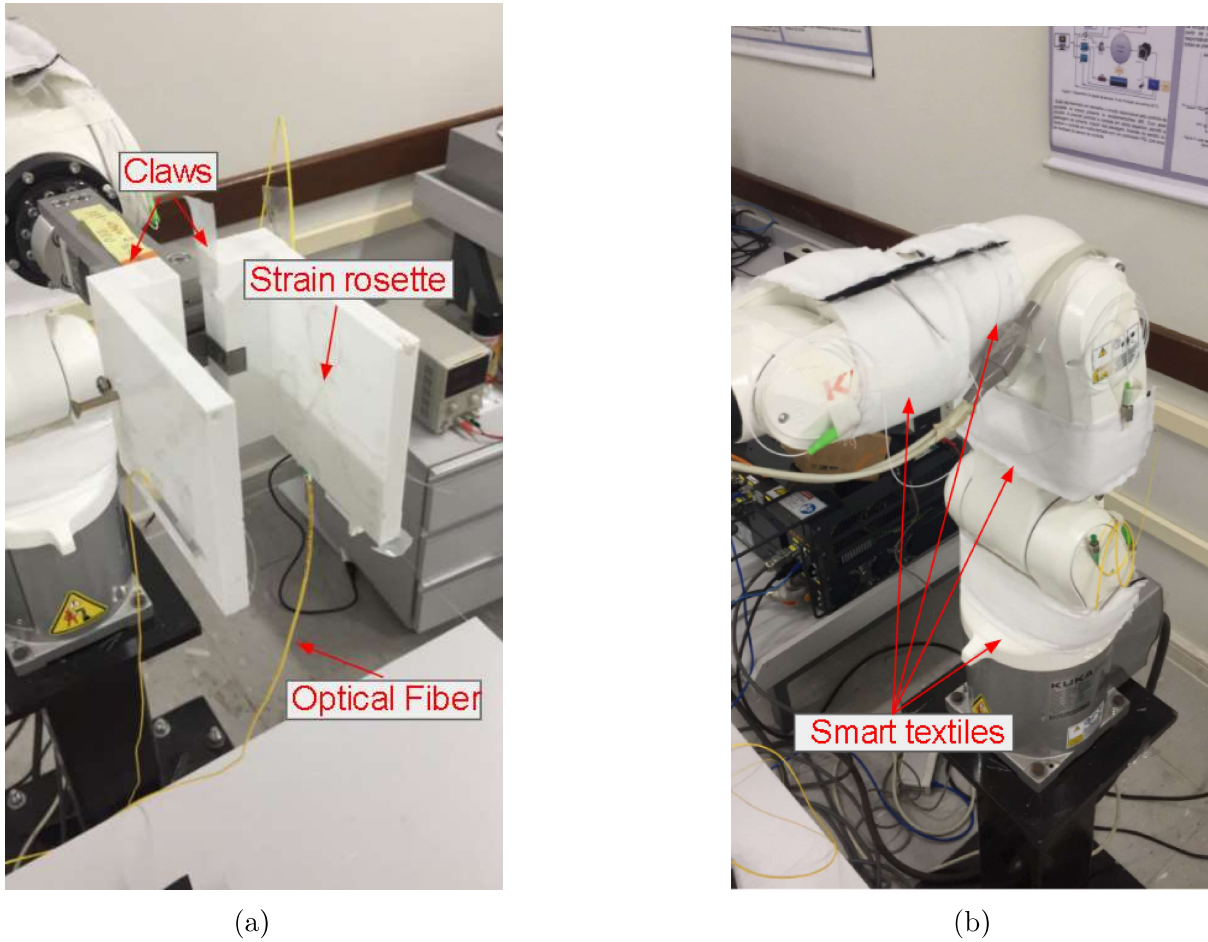


Figure 8 – Proposed sensing systems installed on the robot's body being (a) instrumented claws and (b) tactile system

### 3.2 Test environment presentation

The practical implementation of the instrumented claws and of the tactile system is made seeking to monitor interactions of the robotic manipulator Kuka KR3 R540 (KUKA Industrial Robots, Germany) with the environment and its work objects. The robot is an industrial open kinematic chain manipulator formed by a mechanical system and electrical components. It has 6 Degrees of Freedom (DoF) on its joints and its structural parts are made of cast light alloy. The electrical components include the energy supply systems and all the motors which are used to execute the joint's angular movement. The robot has a mass of 26.5 kg, a workspace volume equal  $0.61\text{m}^3$ , and a maximum reach of 541mm. One of the robot accessories is the 2-finger electric gripper LEHZ20 (SMC, Japan) for the manipulation and transport of objects. The gripper operates with the drive of its servomotor which causes the approximation of the two parallel surfaces on its inner part and the desired object is then gripped. The robot Kuka KR3 in which the sensing systems were tested is available in the Laboratory of Robotics and Biomechanics (CT3 - UFES) where validation experiments were performed.



Figure 9 presents the robot Kuka KR3 and the gripper LEHZ20.

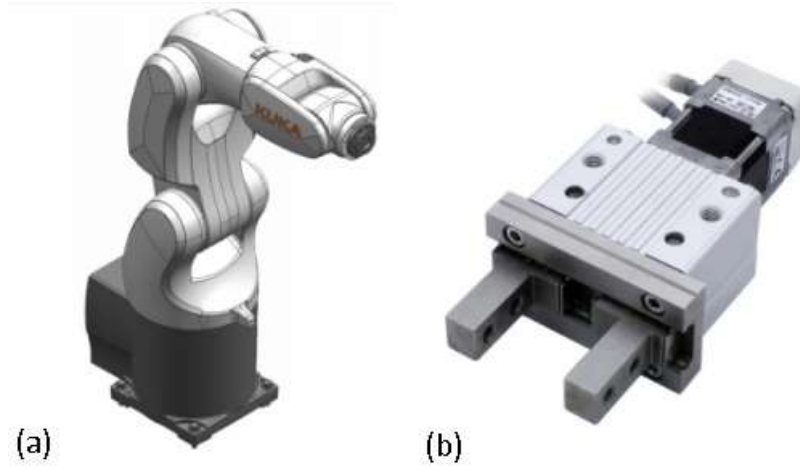


Figure 9 – (a) Robo Kuka KR3 R540 and (b) Electric gripper LEHZ20

### 3.3 Sensors' description and manufacturing setup

All the manufacturing process of the sensors and the instrumented claws was performed in the Associate Laboratory I3N in the University of Aveiro. As part of the prototype of the instrumented claws for stress-strain state monitoring and the tactile system to detect environmental interactions, the single-mode silica optical fibers GF1B (Thorlabs Inc., EUA) are used as the transmission channel for the light. The fiber has a cladding diameter of  $125\ \mu\text{m}$  and a coating diameter of  $250\ \mu\text{m}$ . The sensing elements of the prototype are the uniform FBGs that were inscribed in the fibers through the ultraviolet (UV) laser irradiation with the phase mask technique. For the inscription of FBGs, phase masks (Ibsen Photonics, Denmark) with different periods were used in order to ensure that the central wavelengths of the sensors were different from each other. This prevents the signals from overlapping and affecting the measurement results.

A nanosecond-pulsed Nd:YAG LS-2137U laser (LOTIS TII, Belarus) emitting at  $266\ \text{nm}$  with  $8\ \text{ns}$  pulse time was used to make the gratings inscription. The laser beam is reflected by a set of mirrors to a converging cylindrical lens that directs the beam to a point on the phase mask. A slit was used to control the physical length of the FBGs equal to  $2\ \text{mm}$ . Figure 10 presents a schematic of the components of the phase mask inscription technique and the light path from the laser until coupling to the optical fiber. The fiber coating was removed for FBG inscription, reducing the fiber's mechanical resistance in the regions in which the sensors are positioned. The time exposition was for 10 seconds and the FBG spectrum was monitored with an optical sensing interrogator sm125 (Micron Optics, USA).

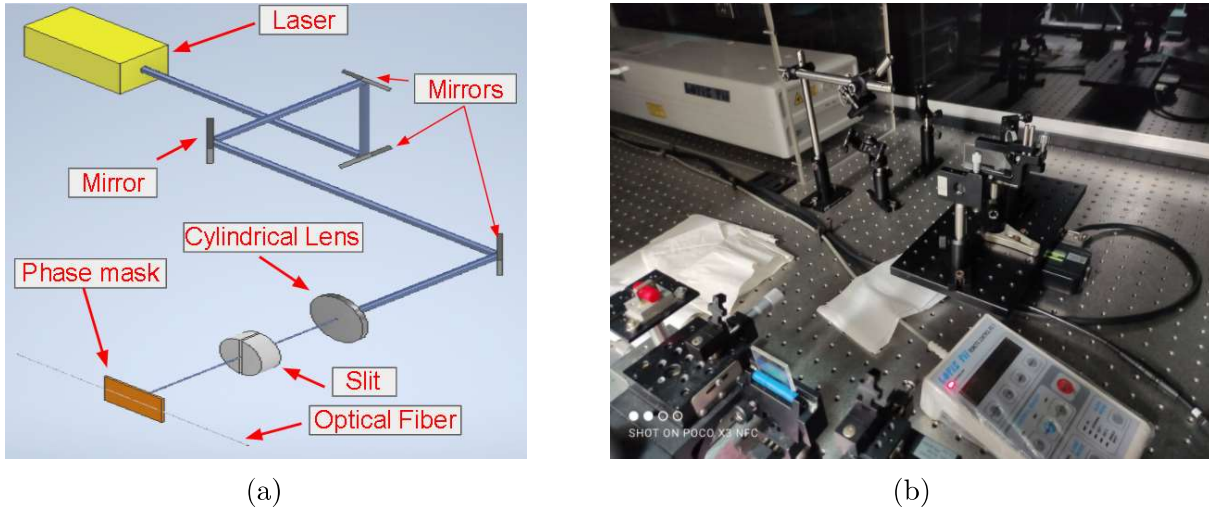


Figure 10 – Phase mask technique for inscription of FBGs (a) schematic and (b) laboratory setup.

### 3.4 Instrumented claws' development

#### 3.4.1 First prototype of the claws

The first prototype of the claws was developed having as its main requirement an adequate region for the installation of the sensors. Since friction is required for the claws to hold the object, the proposed design has dimensional characteristics that were thought to achieve as possible a large area of contact between claws and an object. These dimensions should be limited as a large gripping area associated with a small thickness may produce significant bending on the claws free end putting at risk the structural integrity of the claws. A flat geometry was chosen for the gripping region to ensure that parts with different geometries can be handled. A 2 mm deep slot was made in the gripping region to position the silica fiber with the FBGs on the claws. Due to the silica fiber's brittle behavior when it is mechanically stressed, it was necessary to make curves with a radius of 10 mm at the vertices of the FBG triangular rosette to avoid too sharp bends on the fiber. The 3D design of both parts of the first design was done using the software Autodesk Inventor for posterior manufacturing. Figure 11 presents the front, superior, lateral and isometric views of one side of the claws and its dimensions.

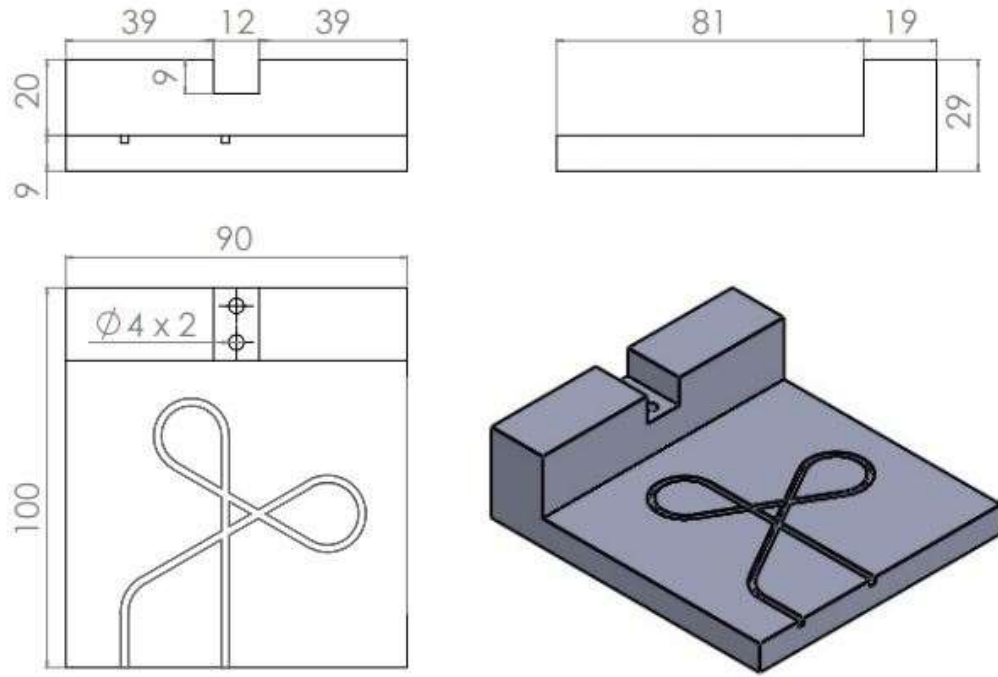


Figure 11 – Claw front, superior, lateral and isometric views.

The claws manufacturing was performed using a Sigma R19 3D printer (BCN3D, Spain). The additive layer manufacturing was selected as the manufacturing process due to its low time consuming and no need for an additional post-fabrication process to do the fixing bolt hole and the deep slit to pass the optical fiber. A force of 40 N is the maximum force of the electric gripper installed on the robot according to the manufacturer's information. For this reason, it is assumed that a 20 percent fill can withstand the force on the surface of the claws and the manufacturing speed tends to be high due to the presence of many voids inside the part. Furthermore, the printing material is polylactic acid (PLA) as it has low cost and a Yield strength of about 70 MPa (FARAH; ANDERSON; LANGER, 2016).

The optical fibers with the FBGs were positioned inside the slot on the center of the claws. One of the fiber ends was cleaved and fused to an Angled Physical Contact (APC) connector using a Fusion Splicer FMS-40S (Fujikura Ltd., Japan) for communication with the optical interrogator and the other end was positioned on the lateral side of the claw to be outside of the loading region avoiding interferences on the signal of the reflection spectrum. The epoxy resin was poured on the slot of the claws and a period of 24 hours was awaited for the material to cure. Figure 12 shows the 3D printer Sigma R19 used in the manufacturing process and the positioning of the FBGs in the right claw for later analysis. Due to the symmetry between the claws, the left claw has a representation similar to the right one.

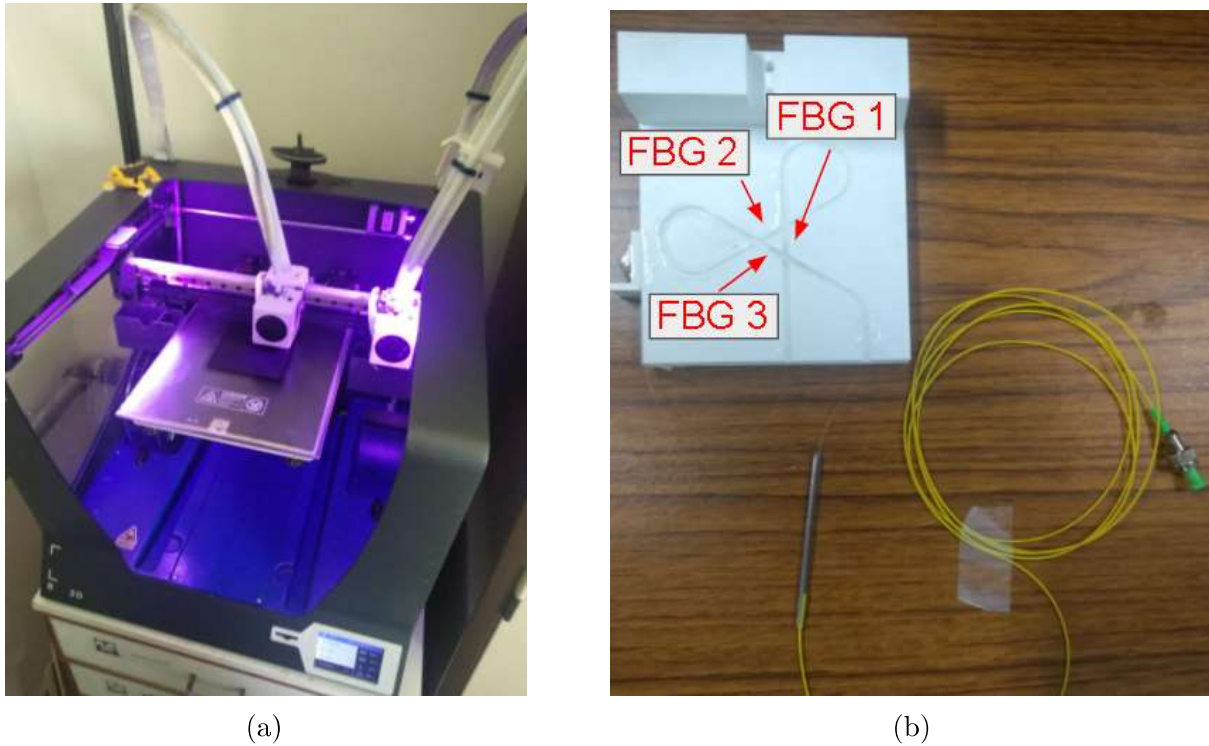


Figure 12 – (a) 3D printer Sigma R19 and (b) Positions of the FBGs on the claw.

### 3.4.2 Second prototype of the claws

In order to more precisely control the positioning of the optical fiber in the claw surface and to avoid the transfer of strain between the FBGs due to curvature effects, another type of design has been thought for the instrumented claw. A rectangular base was designed to receive each of the FBGs that make up the strain rosette. Each FBG is inscribed in a different optical fiber that passes the base through a slot with a depth close to its diameter. The bases take up significant space on the grip surface and therefore it was not possible to use a single fiber for all sensors. A flexible region at the base ends was proposed to act as a strain amplifier by allowing a larger strain of the structure that contains the FBG. For this reason, an increase in the sensor's sensitivity is expected. The FBGs were positioned pre-tensioned between the two strain amplifiers and a small amount of epoxy resin was placed over them. Cyanoacrylate was applied on both sides of the base to ensure its fixation. The second claws design was 3D printed on PLA with the same dimensions as the previous design. Its design features slots so that the three sensor bases and the silica fibers can be positioned together in a delta strain rosette configuration. The signals from the three fibers are connected into a single output using a coupler before going to the optical interrogator. Figure 13 shows the claw 3D design and the manufactured second prototype of the claw.



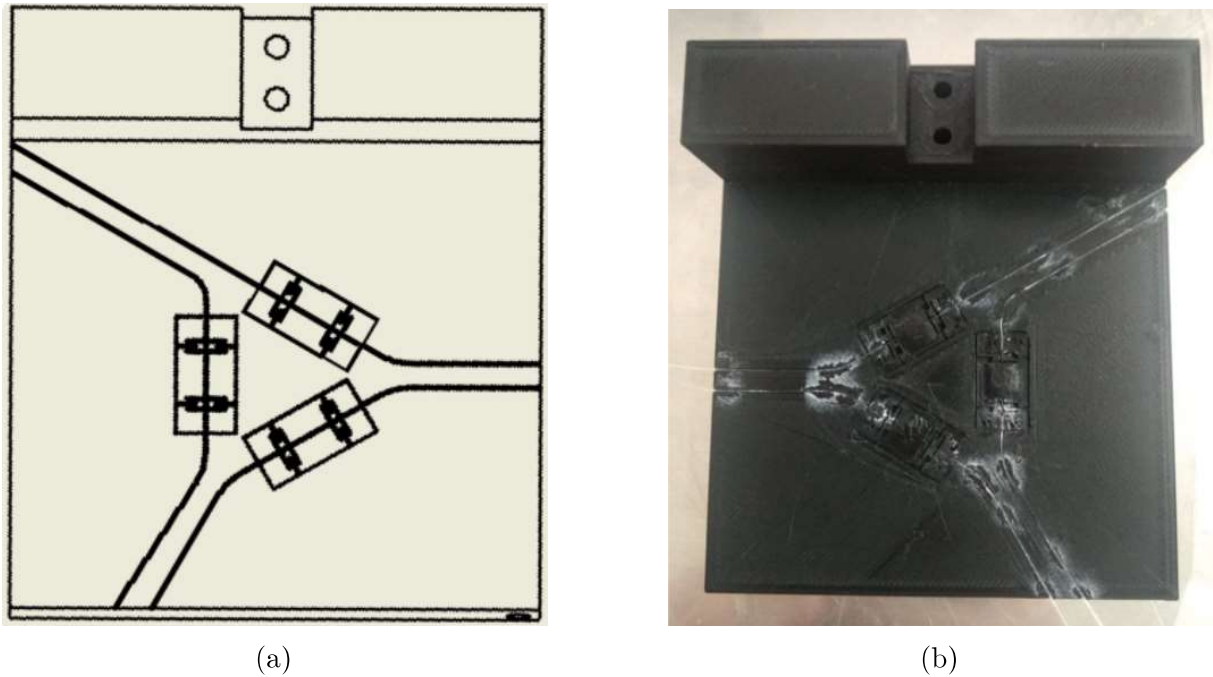


Figure 13 – Second claw (a) 3D design and (b) manufactured prototype.

### 3.4.3 FEM simulation

A numerical static structural analysis was performed through the Finite Element Method (FEM) on the software Ansys Workbench to qualitatively evaluate the distribution of axial strains on the optical fiber and compare them with the experimental compression test. The 3D geometry was the same as the claw's first design plus the epoxy resin and optical fiber on the slot. The selected position for the optical fiber was on the center assuming that it was not possible to guarantee its positioning at the bottom of the slot during the manufacturing process. Boundary conditions were a pressure of 0.0278 MPa applied to the gripping surface of the claw and the surface on the opposite side acting as fixed support. The boundary conditions were chosen to be similar to the characteristics of the compression test and to produce strains greater than the FBG resolution (Figure 14).

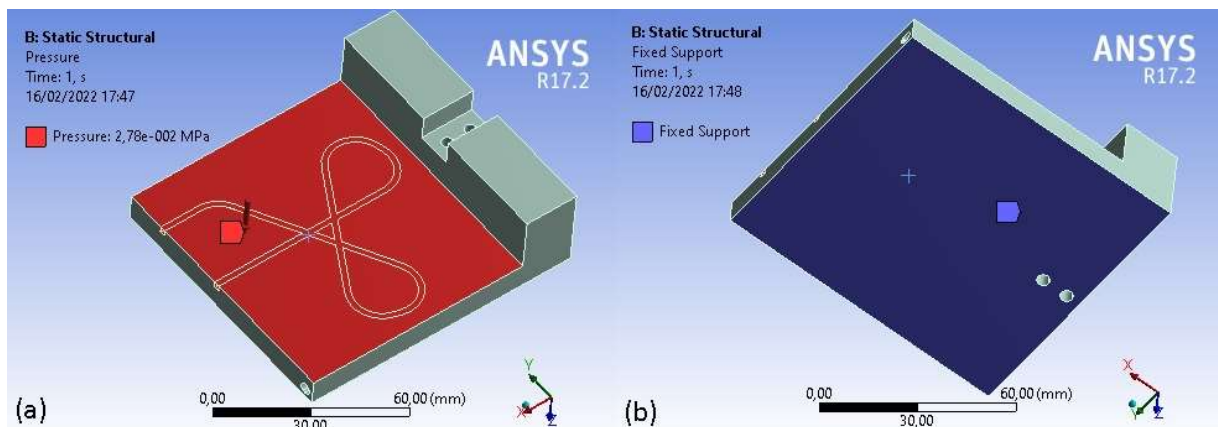


Figure 14 – Boundary conditions (a) distributed pressure and (b) fixed support.

Table 1 shows the mechanical properties of the materials of the simulation. The materials were considered to have isotropic elasticity.

Material	Young's Modulus (GPa)	Poisson's Ratio
PLA	3.0	0.33
Silica optical fiber	70	0.17
Epoxy resin	0.0016	0.48

Table 1 – Mechanical properties of the materials from numerical analysis

The generated mesh had 342487 nodes and 217069 discrete elements. The accuracy of the FEM depends on the number of nodes and discrete elements, as well as the mesh size. The smaller the mesh size and the greater the number of elements in a given mesh, the greater the accuracy in the analysis results. Three auxiliary coordinate systems were built in FBGs direction to be possible to obtain the longitudinal strain which supposedly shifts the Bragg wavelength.

#### 3.4.4 Temperature and strain characterization

After the fabrication process, the sensors were characterized in terms of strain and temperature variation to obtain the relation of the wavelength shift with these parameters. Figure 15 presents the experimental setup for the temperature characterization of the claws.



Figure 15 – Experimental setup for FBGs characterization to temperature variation.

The 3D printed claws with the FBG sensors of the first prototype were positioned inside of a thermal chamber LabEvent (WeissTechnik, Germany) and the reflection spectrum of the optical fibers was monitored using the interrogator sm125 to obtain the wavelength shifts with temperature variations. The chosen temperature range is from 20 to 45°C with increments of 5°C. The wavelength shift for each temperature point was collected after 30 minutes as thermal systems have a high time constant and consequently a slow transient response (RABBANI et al., 2013). The tests were performed for the left and right sides of the claws from the first design separately.

Due to the geometric irregularities of the first claws, it is not feasible to perform the tensile testing to characterize the FBGs to axial strain after fabrication and positioning them in the claws. A reference FBG embedded in a volume of epoxy resin similar to one of the claws FBGs was used to approximate the sensitivities of the sensors to axial strain. Figure 16 presents the setup used in the experiment.

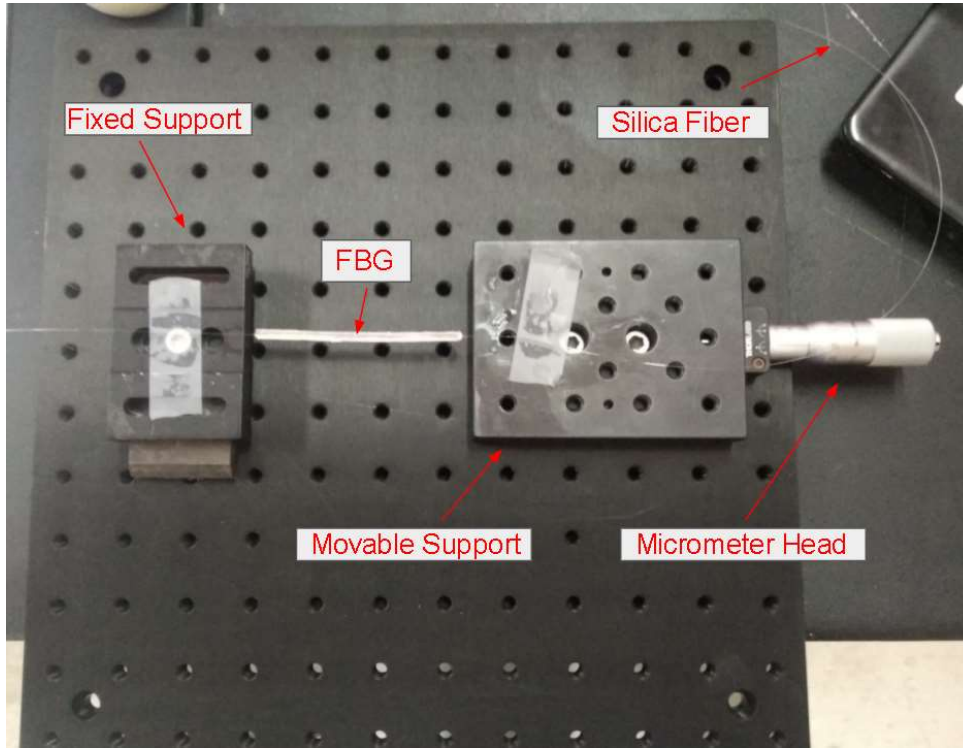


Figure 16 – Experimental setup for FBGs characterization to axial strain.

The fiber region with the FBG was positioned as a simply supported beam with one end on a fixed support and the other end on a movable support. A micrometer head is used to displace the movable support and to produce an axial strain on the fiber resulting in a Bragg wavelength shift to be monitored with the optical sensing interrogator sm125. The data was collected for the displacement of movable support varying from 0 to 0.16 mm with increments of 0.02 mm. To ensure statistical precision, the tests were done five different times. The axial strain was obtained as the division between the displacement of the movable support and the initial distance between the fiber attachment points. It was necessary to control the forces and stresses applied on the silica fiber during the tests to avoid damages as it presents a brittle nature without external protection.

For the second design, the characterization to strain was done for the three FBGs separately before inserting them into the claw slots. The same setup as in Figure 15 was applied. The micrometer increments were 0.02mm with a range varying from 0 to 0.16mm and the tests were repeated three times for each one of the FBGs of both claws to ensure sensitivity values with greater statistical accuracy. Again, the strain was indirectly calculated as the division between the displacement of the movable support and the initial distance from the optical fiber attachment points to the fixed and movable supports. On the next step, the sensor bases were then glued to the claws to proceed with the temperature characterization. The temperature tests were performed using the same experimental setup and parameters which were applied previously in the Figure 16.



### 3.4.5 Compression tests

After characterization, compression tests were performed on the Universal Testing Machine AGS-5kND (Shimadzu, Japan) to verify the sensors' behavior and if the claws can handle compressive loads. Figure 17 shows the setup and equipment used on the compression test.

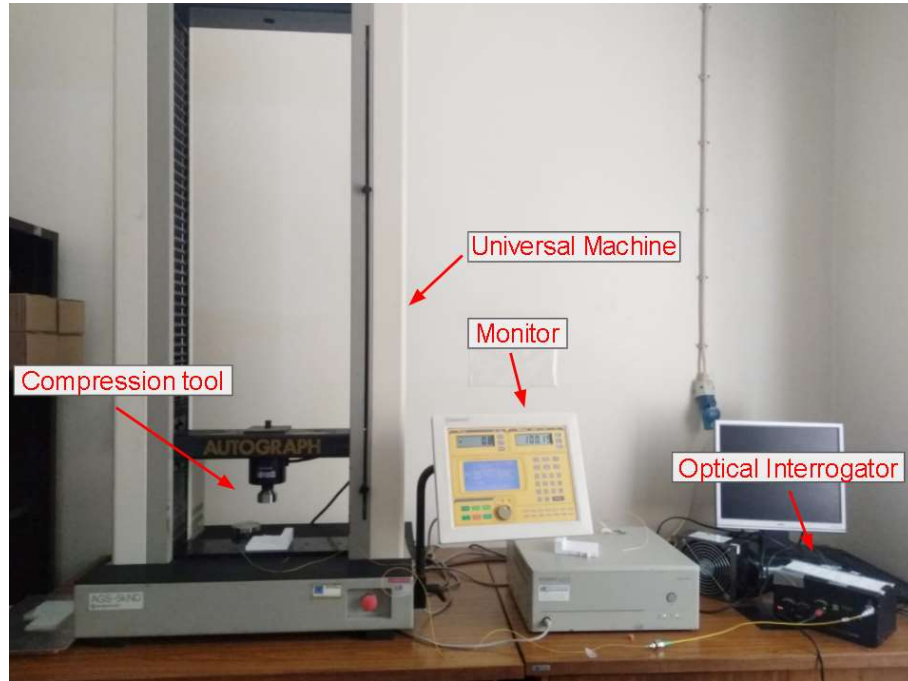


Figure 17 – Experimental setup of the compression tests.

The claws from the first prototype were positioned over a base parallel to its gripping surface and a force was applied on it perpendicular to the longitudinal axis of the optical fiber by the compression tool. The force ranges from 0 to 100 N with increments of 10 N, however the machine's load cell does not have good accuracy with respect to load measurement. For this reason, the load applied in the tests for the left and right claws differed minimally from each other. Even though the maximum force value of the gripper is equal to 40 N, tests with higher force values were carried out to assess whether the dynamic range of the sensors is suitable for application in tools with load capacity superior to 100 N. The wavelength shift on the reflection spectrum of the FBGs was monitored using the optical sensing interrogator sm125 and the compression load was monitored on the machine's display. The calibration curve obtained from the characterization to axial strain was used to obtain strain values from wavelength shift.

For the second prototype, the compression tests were done using the same setup. In this case, the applied forces range from 0 to 200 N with increments of 10 N up to 40 N, which is the maximum load that can be applied by the robot gripper, and with increments of 20 N up to 200 N. The maximum load value was been increased up to 200N due to a

more rigid structure of the claws observed by the lower sensitivity of the sensors when compared to the first design.

When a linear elastic material undergoes a transverse deformation then a longitudinal deformation is induced in the same material due to the Poisson effect. The compression load causes a negative transverse strain and consequently, a positive longitudinal strain on the FBGs and for this is expected positive values for wavelength shift on the FBGs.

### 3.4.6 Experimental validation

The experimental validation of the instrumented claws in the manipulator consists of measuring the strains in the strain rosette sensors while the robot captures an object on a table. The strain values obtained from the tests can be used to obtain the critical strains and stresses from the Eq. 2.7-2.36. Thus, it is possible to assess whether the design limits are being exceeded during service. The instrumented claws were fixed to the gripper LEHZ20 using screws and nuts. When the gripper is on, the claws capture the object and when the gripper is off, the claws release the object. After the claws installation on the robot gripper, the optical fibers from each claw were connected to the optical interrogator HYPERION si255. Figure 18 shows a scheme of the proposed instrumented claws after installation on the robot.

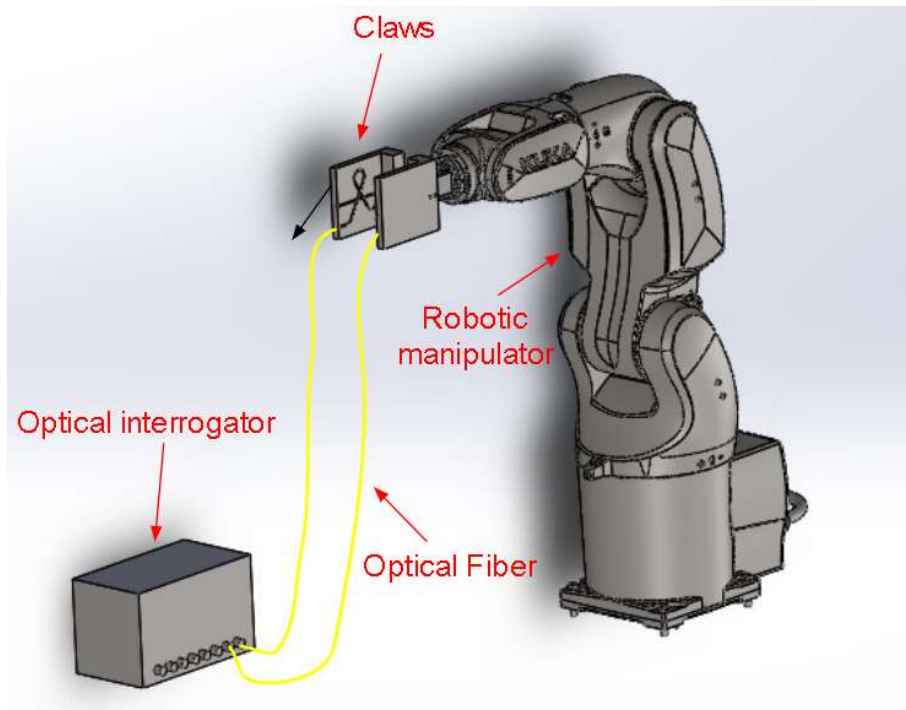


Figure 18 – Claws sensing system installed on the robot.

This optical interrogator was selected due to its maximum sampling frequency of 1 kHz which is sufficiently faster to save the data of the robot's movements at the desired times. The wavelength accuracy of the interrogator is equal to 1 pm and consequently,

the system resolution is equal to  $1.23 \mu\epsilon$ . Moreover, this interrogator was eight available optical channels for data collection which allows the simultaneous operation of the tactile sensor system and the instrumented claw. The robot's main movements during the tests consisted basically of:

- (1) approach a table and grab an object positioned on it.
- (2) return to the starting position holding the object.
- (3) return to the table and put the object on top of it.

Two objects were used on the tests: (i) a quadrangular prism with dimensions of 58.64 mm x 85.20 mm x 123.60 mm and weight of 135.046 g; and (ii) a cylinder with a diameter of 57.70 mm, a height of 271.00 mm and a weight of 228.196 g.

The experiment was carried out three times for each object with the robot tool center point at a speed of 250 mm/s. The reflection spectrum of the optical fibers was collected using the optical interrogator in three different moments. The first moment is when the robot is in the initial position of the trajectory (point 0), the second one is immediately after the robot grabs the object on the table (point 1) and the final one is immediately after the robot puts the object on the table (point 2). Figure 19 presents the three points of the robot's trajectory in which the data is collected.

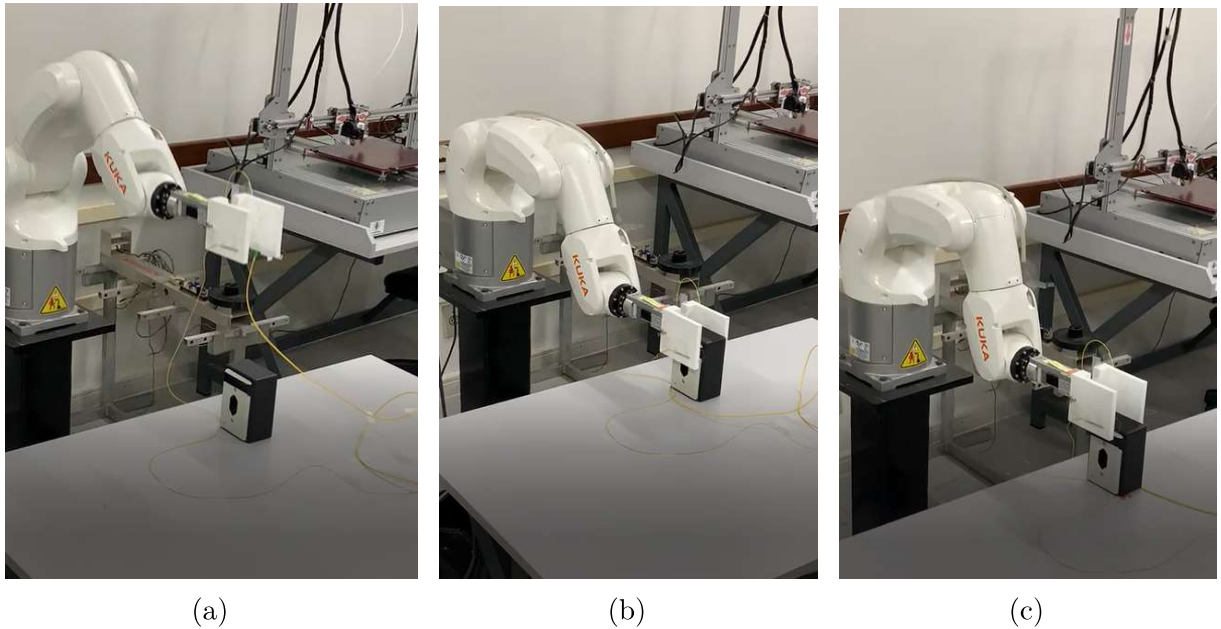


Figure 19 – Data collection points in instrumented claws validation experiments (a) point 0, (b) point 1 and (c) point 2.

A coordinate system is used as the basis for the stress and strain calculations at the center point of the claw where the FBG strain rosette is positioned. Figure 20 presents the position and orientation of the Cartesian coordinate systems on the right and left claws.  $\epsilon_a$  is the strain on the FBG 1 for both claws,  $\epsilon_b$  is the strain on the FBG 2 for the

left claw and the strain on the FBG 3 for the right claw and  $\epsilon_c$  is the strain on the FBG 3 for the left claw and the strain on the FBG 2 for the right claw.

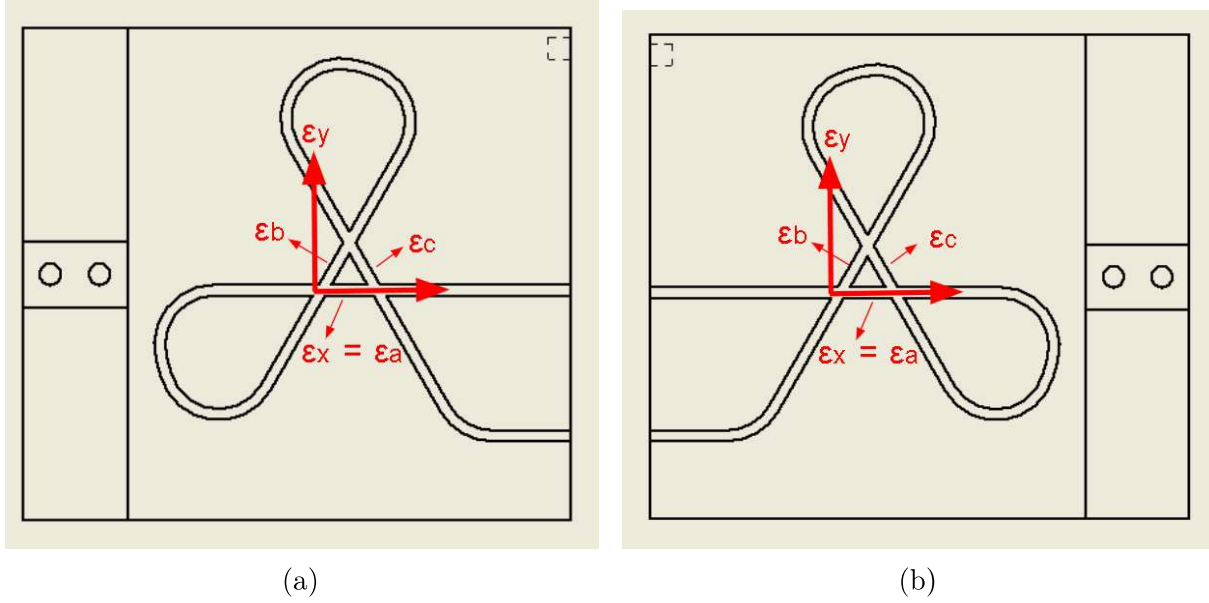


Figure 20 – Coordinate systems on (a) the left claw and (b) the right claw.

The results were then used as a reference to plot the strains obtained from the previous characterization of the FBGs and the critical stresses and strains after the transformation equations.

### 3.5 Tactile system's development

For the tactile contact detection system, it is proposed to use a set of optical fibers positioned circularly around the robot's links. In each fiber, a series of FBGs multiplexed is installed so that each sensor covers a part of the link where the optical fiber is positioned. The interactions between the environment and the robot tend to act on the optical fibers as transverse loads. By approaching the behavior of the fiber as a beam under bending, from the geometric characteristics and properties of the materials, the distance between the sensors can be estimated so that the system has a useful sensitive area. A mathematical model is proposed to meet this requirement before refining the mechanical structure of the system. All the manufacturing process and characterizations of the tactile system was done in the Dynamics Instrumentation Laboratory (CT3 - UFES).

#### 3.5.1 Mathematical model to estimate the distance between sensors

To achieve a tactile sensing system capable of detecting mechanical touches in many points on the surface of the robot's body, it is necessary to determine the minimal distance between the FBGs and consequently the number of FBGs. The optical fibers from

the sensing system undergo a bend when an external stimulus is applied transversely to its axis due to the existence of the substrate between it and the robot body. A reasonable model to consider this is the simply supported beam model with a concentrated load applied at a generic distance  $x$  from the first support. Figure 21 shows the main parameters that are important to solve the model.

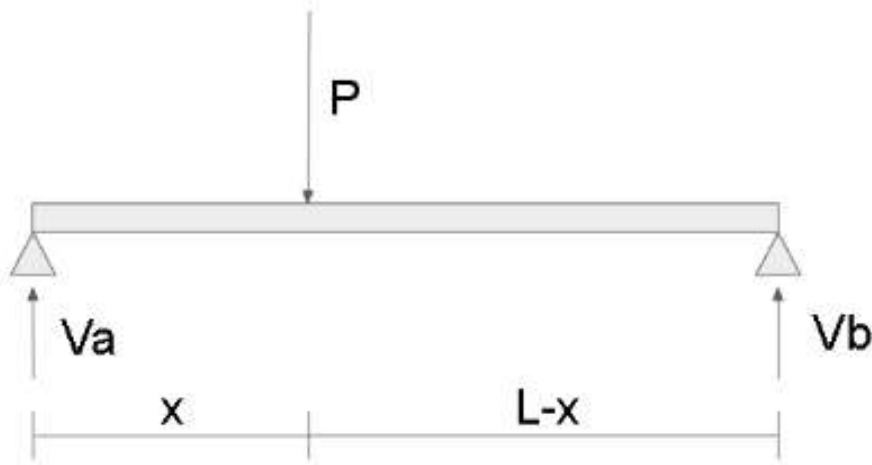


Figure 21 – Parameter of the simply supported beam with a concentrated load.

$L$  is the length of the optical fiber,  $P$  is the interaction/contact force and  $V_a$  and  $V_b$  are the reaction in the supports. The definition that the sum of forces and moments at a point on a static rigid body are equal to zero is used to obtain the supports reactions.

The curvature of the fiber due to the interaction with the environment causes the appearance of internal bending moments that vary along the fiber longitudinal axis. The presence of these internal moments results in strains on fiber longitudinal direction that causes wavelength shifts on the FBGs used on the tactile system. For the configuration of Figure 21, the internal moment along the fiber length may be defined by Eq. 3.42.

$$M(a) = \begin{cases} \frac{-P \cdot x \cdot a}{L} + P \cdot a, & 0 < a < x \\ \frac{-P \cdot x \cdot a}{L} + P \cdot x, & x < a < L \end{cases}, \quad (3.42)$$

It can be guaranteed that the system is detecting a contact when the FBG closest to the load presents a shift in its central wavelength. This consideration is feasible because this FBG is under the highest values of stress due to bending. Assuming that all FBGs are on the same distance from each other and being  $c$  the distance between two adjacent FBGs, the FBG immediately to the left of the force  $P$  is positioned in a distance of  $x - \frac{c}{2}$  from the left support and the FBG immediately to the right of the force  $P$  is positioned in a distance of  $x + \frac{c}{2}$  from the left support. Then, the bending moment on the FBGs immediately to the left and right of the concentrated load is given by the Eq. 3.43 and

3.44, respectively.

$$M_l = \left(\frac{x}{L} - 1\right) \cdot \left(\frac{P \cdot c}{2} - P \cdot x\right), \quad (3.43)$$

$$M_r = P \cdot x \cdot \left(1 - \frac{x}{L} - \frac{c}{2L}\right). \quad (3.44)$$

The maximum fiber deflection is limited by the thickness of the substrate over which it is positioned. For this reason, the fiber suffers small deflections and its behavior can be modeled by applying the elasticity theory. Considering that the material properties are isotropic and the material has linear elastic behavior, the bending stresses on the fiber are related to the bending strains by Hooke's Law. Knowing that the optical fiber cross-section is circular, the longitudinal strain at the point farthest from the neutral line as a function of the internal bending moment is presented in Eq. 3.47.

$$\epsilon = \frac{32 \cdot M}{\pi \cdot E \cdot d^3}. \quad (3.45)$$

where  $\epsilon$  is the bending normal longitudinal strain,  $E$  is the Young's Modulus of the optical fiber and  $d$  is the diameter of the optical fiber. Due to the symmetry in the fiber and for simplification purposes, it was decided that only the analyzes for the FBG on the left side of the load are sufficient. As the longitudinal strain equations are parabolic, the smallest strains are in the FBGs on the fiber ends. Ensuring that the region with the least strains reaches the minimum resolution of the FBG then the other regions also reach. Considering the first FBG positioned at  $\frac{c}{4}$  of the fiber left end, the maximum strain value on it is given by Eq. 3.46.

$$\epsilon_{min} = \frac{8 \cdot P \cdot L \cdot c - 6 \cdot P \cdot c^2}{\pi \cdot E \cdot d^3 \cdot L}. \quad (3.46)$$

The value of the concentrated load at a distance  $x$  from the left support of a simply supported beam that can be applied to achieve the maximum deflection of the fiber is given by Eq. 3.47.

$$P = \frac{\pi \cdot \epsilon_{max} \cdot E \cdot d^4 \cdot L}{8 \cdot \left(L \cdot c - \frac{3 \cdot c^2}{4}\right) \cdot \left(L^2 - \frac{9c^2}{16} - \left(L - \frac{3c}{4}\right)^2\right)}. \quad (3.47)$$

When this force value is reached, the fiber begins to undergo a transverse deformation (as shown in Figure 22) that affects the longitudinal deformation of the fiber by Poisson's effect.

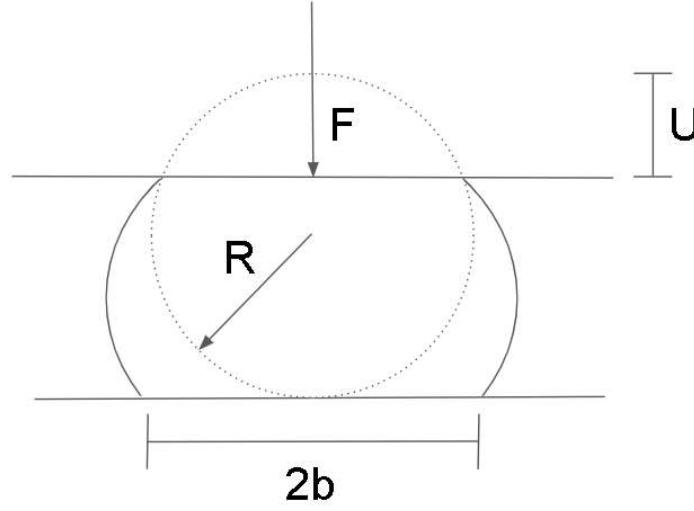


Figure 22 – Representation of the fiber undergoing a transversal deformation.

where  $F$  is the force per unit length,  $2b$  is the contact width,  $U$  is the diametric compression and  $R$  is the radius of the cylinder. The work from Hillbrick et al. (2019) provides some models to calculate the cross-section deformation of a cylinder compressed between two flat plates. Extending the approach to the optical fiber, the half contact width is obtained from Eq. 3.48. The model from Lundberg e Yhland (1949) was chosen for the relative displacement between two flat plates (Eq. 3.49).

$$b = \sqrt{\frac{2 \cdot F \cdot d}{\pi} \cdot \left( \frac{1}{Et} - \frac{\nu^2}{E} \right)} \quad (3.48)$$

$$U = \frac{4F}{\pi} \cdot \left( \frac{1}{Et} - \frac{\nu^2}{E} \right) \cdot \left( \ln\left(\frac{d}{b}\right) + \frac{1}{3} \right) \quad (3.49)$$

$Et$  is the transversal modulus of the optical fiber. The transverse deformation of the fiber also has an effect of longitudinal deformation on the fiber length. Eq. 3.50 provides the strain on the FBG on the extremity of the fiber.

$$\epsilon = \epsilon_{min} + \nu \cdot \frac{U}{d} \quad (3.50)$$

The mechanical properties of the silica fiber were obtained from the works of Díaz et al. (2017) and Wierzbza e Kosmowski (2003). The lower touch sensitivity of the human skin happens in the forehead and in the palm and is equal to 0.7 mN (ACKERLEY et al., 2014). Unlike a human, robotic manipulators have high robustness and inertia and a low magnitude force should be insufficient to compromise their movement. For this reason, it can be assumed that the tactile system does not need a touch resolution as low as human skin.

Assuming that the lower strain detected by the sensors is the strain resolution of a 2mm length FBG (from the work of Tahir et al. (2011)), it is possible to obtain the average distance between FBGs from the proposed model. Table 2 presents the geometric characteristics of the optical fiber and the mechanical properties used on the model to evaluate the distance between FBGs in the tactile system.

Characteristics	Silica optical fiber
Young's Modulus (GPa)	70.0
Poisson's ratio	0.17
Fiber diameter (mm)	0.245
Lower force value (mN)	0.7
Fiber length (mm)	600
Strain Resolution ( $\mu\epsilon$ )	10

Table 2 – Optical fiber characteristics for estimating the distance between FBGs

The distance obtained from the mathematical model is equal to approximately 60 mm. Due to the limitations related to the high cost of fabrication of the FBGs and availability of phase masks in the laboratory, it was necessary to reduce the number of sensors obtained from the mathematical model and, consequently, the spatial resolution of the system.

### 3.5.2 Constructive characteristics of the tactile system

Figure 23 presents a scheme of the nomenclature used to refer to the sensors of the tactile system. The links with the textiles were numbered from 1 to 4 starting from the closest to the end effector and the FBGs in each fiber were numbered in ascending order with the first one being the closest to the APC connector. The numbers under the dotted lines represent the distance between the FBGs. The dimensions and positions on the robot's links of each smart textile can also be seen in the Figure 23.



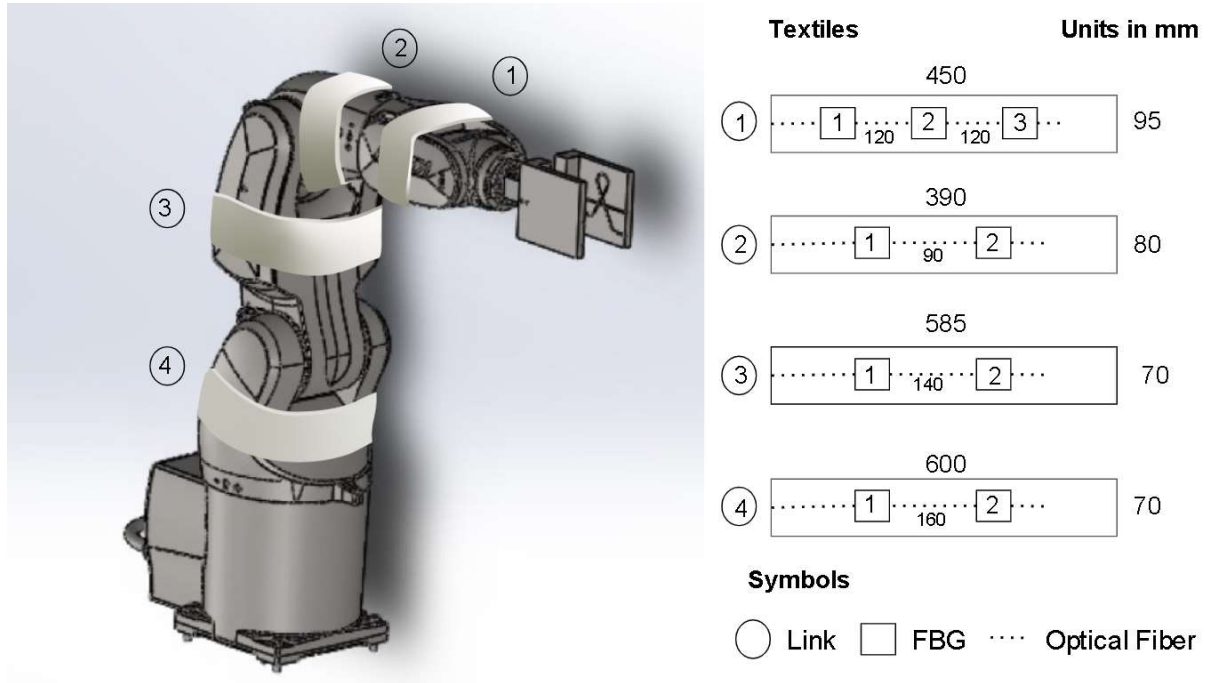


Figure 23 – Nomenclature used for the smart textiles and FBGs installed on the robot's body.

It was chosen to position the optical fibers far from the robot's joints, where the deformations are critical, in order to avoid the optical fibers rupture. Therefore, four fibers are needed, one for each link, to cover the regions of the robot's body most exposed to interactions with the environment. The perimeter of the links was measured so that it was possible to dimension the fibers for each one of them. The link closer to the end effector tends to be more susceptible to external stimuli and, therefore, is equipped with a greater number of sensors.

To improve the mechanical resistance and robustness of the sensors, the regions of the optical fibers with the FBGs were embedded in a small volume of cured silicone rubber. The sensors were positioned on supports made with the Liquid Crystal Display (LCD) based Stereolithography (SLA) 3D printer Photon (Anycubic, China) and then the liquid silicone rubber mixed with 10 percent by mass of catalyst was poured into the supports. It was waited for 24 hours to ensure that the curing process was complete. One end of the fibers has been cleaved and joined to APC connectors so that the reflection spectrum can be monitored with an optical interrogator.

Each one of the smart textiles is formed by an inner layer of two polyethylene foams between which optical fibers are positioned for greater mechanical protection. The polyethylene foams are then sewn between two external layers of cotton fabric. Touch fasteners were glued to the textile ends to be possible to attach the sensing system to the robot's body. Figure 24 shows the internal construction of the smart textile positioned on the link 1.

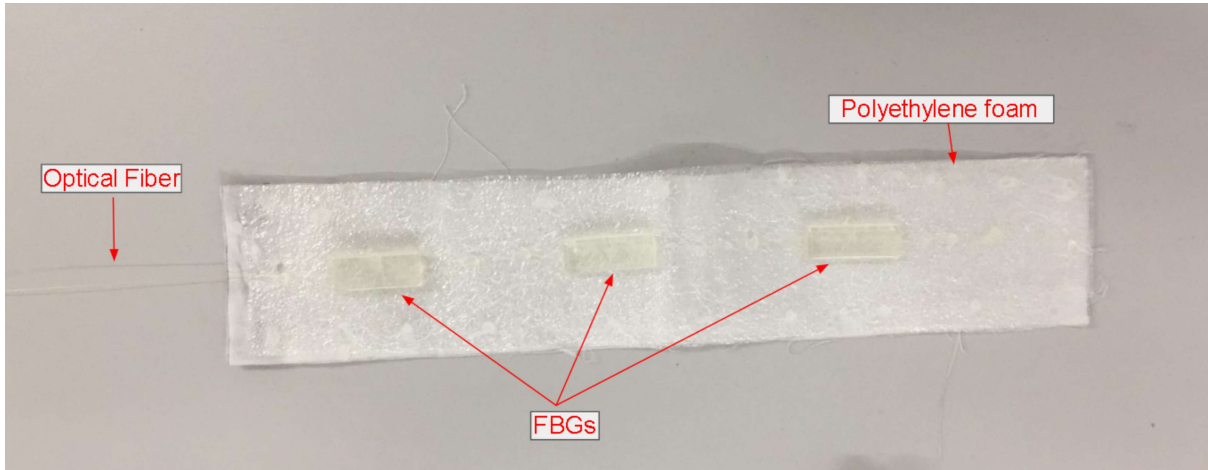


Figure 24 – Internal components that make up the smart textiles.

### 3.5.3 Temperature and force characterization

After the manufacturing process of the smart textiles, tests were carried out for each sensor of the tactile system to obtain their sensitivity to temperature variation and force. The smart textiles were positioned inside the climatic chamber Q315C21N (Quimis, Brazil) and the reflection spectrum of each optical fiber was monitored with the optical interrogator HYPERION si255 (Luna, USA). The temperature selected as a reference to calculate the wavelength shifts of the FBGs was equal to 25 °C. The range of temperature for the tests was from 25 °C to 45 °C with increments of 5 °C. Once reached, each temperature was held for 5 minutes to ensure stability and then the spectra data were saved. A small offset was present in relation to the desired set-points presumably due to the inaccuracy of the climate chamber controller. From the saved data was possible to obtain the curves that correlate the central wavelength shifts of each FBG with temperature variations.

For the force characterization, the FBGs of the smart textiles were positioned separately on the Universal Machine (Biopdi, Brazil) base and a compression tool was installed on the machine to apply the compression forces on them. The machine is equipped with a load cell to measure the force values during the experiments. The force values ranged from 0 N to 50 N with increments of 10 N and the reflection spectra of the FBGs were collected with the interrogator HYPERION si255. Due to the relaxation effects that occur in the viscoelastic materials that make up the structure of the sensors, the force values measured in the machine showed a real-time decrease. It was necessary to wait one minute for force stabilization at each measured point. All the force characterization tests were done in an environment with controlled temperature. Figure 25 presents the universal machine used during the force characterization of the smart textile sensors.

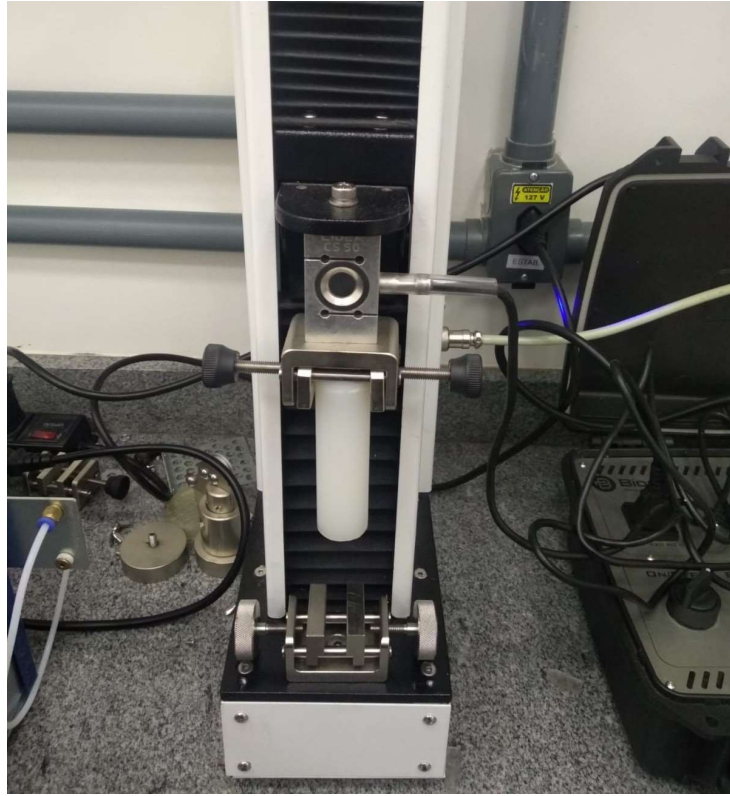


Figure 25 – Universal test machine for the force characterization experiments.

#### 3.5.4 Experimental validation

To evaluate the performance of the tactile system, a set of experiments was proposed. Each smart textile was circularly fixed to the respective link of the robot using the touch fasteners. Initially, the behavior of the sensors was observed while the manipulator performed a trajectory without external interference and, then, it was compared with the response of the sensors when the robot is hit by a rubber mallet. From the disturbances that appear in the signal of the FBGs, it is possible to know the instant that the impact occurred and the location of the robot's body that was hit. Figure 26 shows a scheme of the proposed tactile system after installation on the robot.

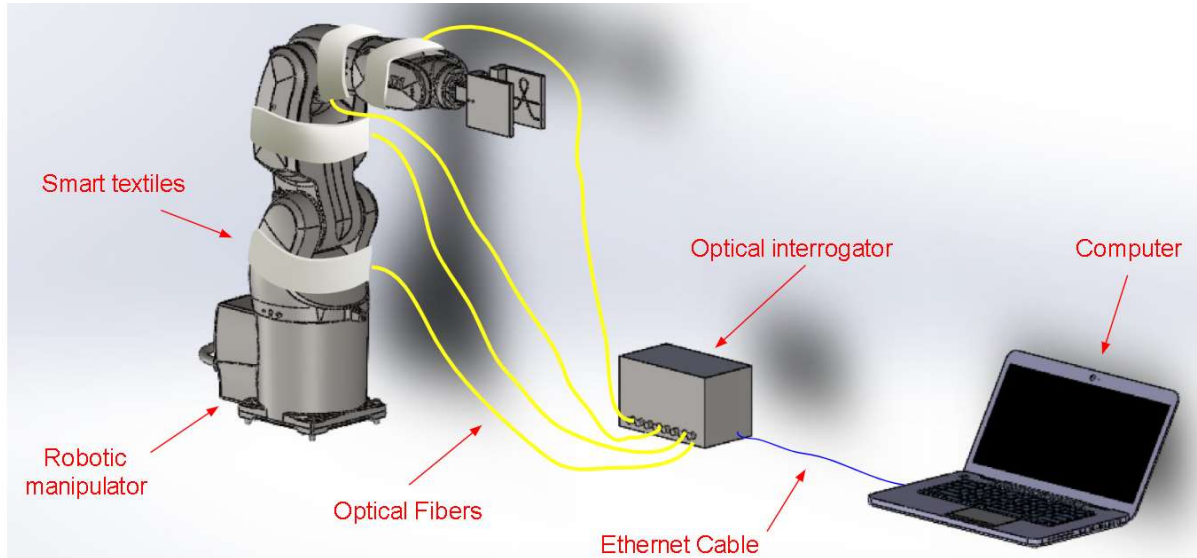


Figure 26 – Tactile sensing system installed on the robot.

The smart textiles were placed on the robot links and the optical fibers were plugged in different channels of the interrogator HYPERION si255. An Ethernet cable is used for communication between the interrogator and a computer for processing the FBGs' data. Since the impacts done with the rubber mallet on the robot body occur in an extremely low time interval, it is necessary a high sampling frequency to avoid loss of relevant data. The trajectory followed by the robot during the tests was the same as previously implemented for the claws test, however, there was no object to be gripped in this situation.

Three different tests were executed for validation of the tactile system:

- (1) execution of the proposed trajectory without any external interference.
- (2) execution of the proposed trajectory with the left side of the robot being hit by the hammer.
- (3) execution of the proposed trajectory with the frontal side of the robot being hit by the hammer.

Each test was executed three times with the end effector at a speed of 250 mm/s and the spectra peaks were saved during the robot's movements with a sampling frequency of 1kHz. In each repetition of the three tests, the impacts on the FBGs on the left and front sides of the robot's body were given in random sequences and time instants. Temperature was controlled in a constant value of 25°C during the experiments.

All tests detailed in this chapter were performed in the laboratory and the next section shows the results obtained. The characterization curves and the experimental validation of the sensing systems are presented and discussions about their behavior are made.

## 4 Results and discussion

This chapter presents the results of the proposed characterization and validation experiments of the instrumented claw and the tactile system. General discussions about the behavior of sensors are also raised and relevant points can be highlighted for future work.

### 4.1 Instrumented claws's simulation and experimental results

#### 4.1.1 FEM analysis

Figure 27 shows the axial strain field on the epoxy resin in the direction of each FBG obtained from the FEM simulation of the first claw left side.

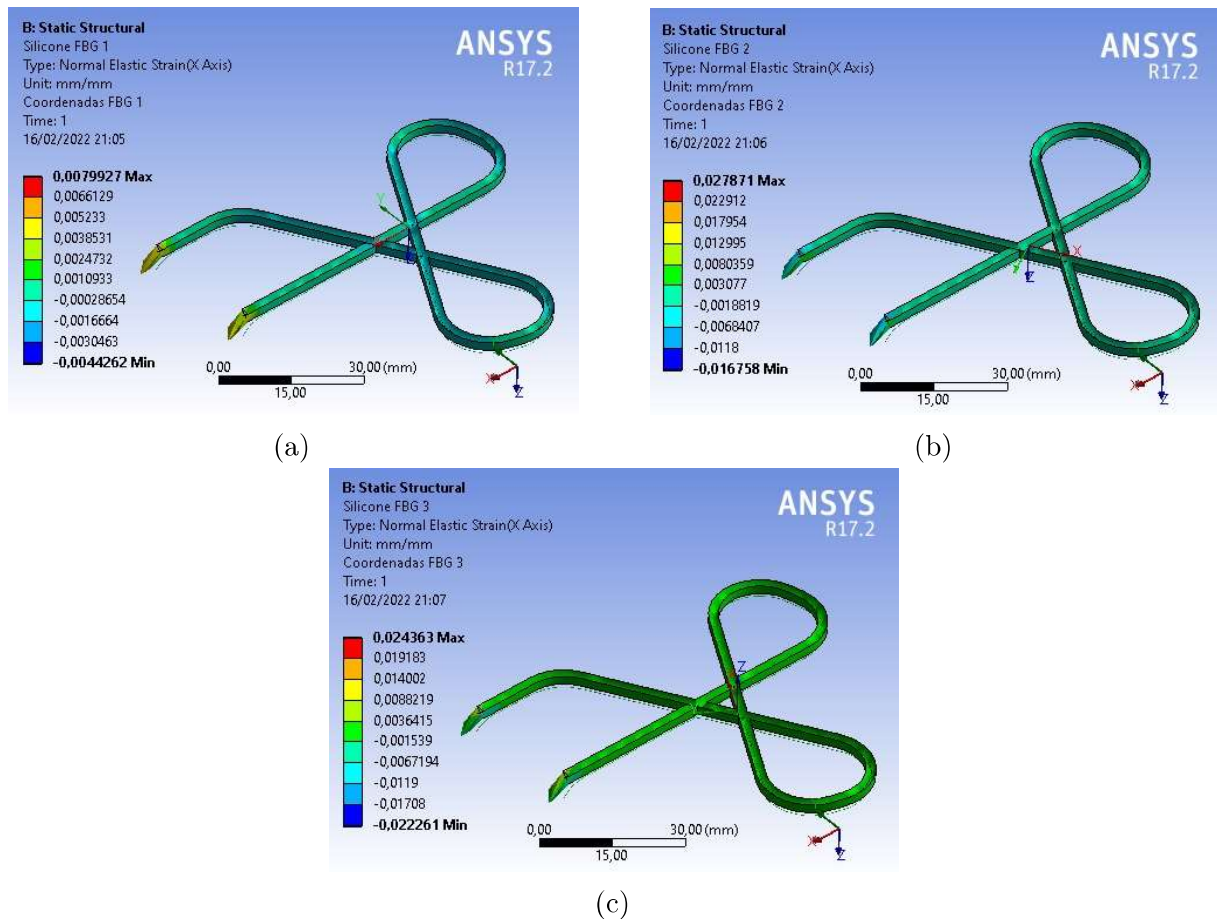


Figure 27 – Strain field on the epoxy resin from FEM simulation for (a) FBG 1, (b) FBG 2 and (c) FBG 3.

The x-axis of the coordinate systems is parallel to each FBG of the rosette and the strains are measured relative to them. The presence of nonuniform strain fields at the



three directions indicates the presence of bending as expected. As the strains along the epoxy resin are almost all compressive, it is therefore expected from the results that the optical fiber is located in the compressive region of the bending and that the wavelength shifts are for lower values.

#### 4.1.2 Temperature characterization

Figure 28 show the points collected during the temperature experiments and the linear models adjusted for each FBG on the left and right claws of the first prototype.

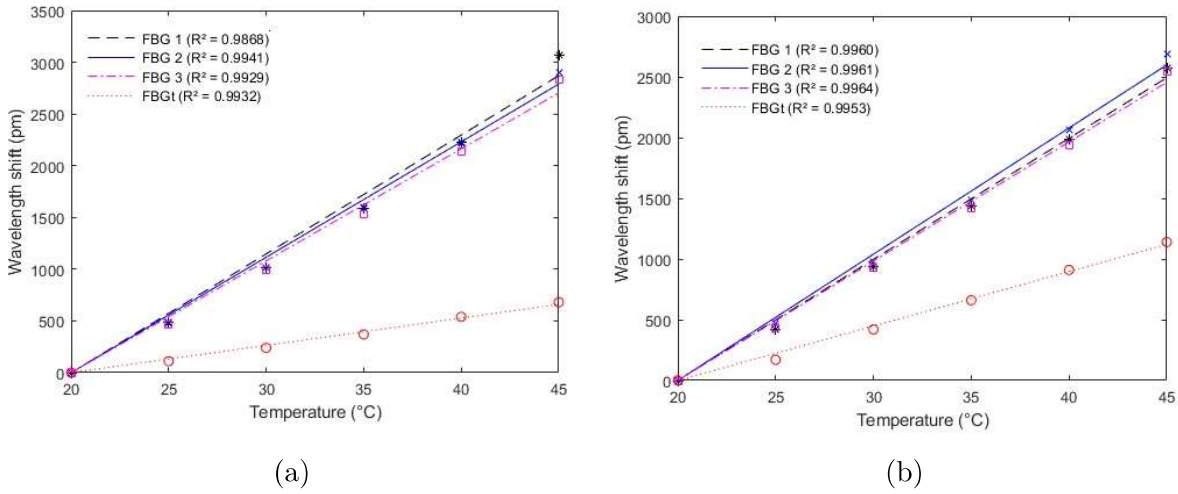


Figure 28 – Temperature characterization of the FBGs from the first design for (a) left claw and (b) right claw.

As expected from the FBG model in the literature, the wavelength shift has a highly linear behavior under the effect of temperature variation. The lower  $R^2$  between the linear regressions of the left and right claws of the first design are 0.9868 and 0.9953, respectively, proving the high linearity of the FBGs to temperature.

The thermal expansion of the epoxy resin induces strains on the FBGs which increase the temperature sensitivity in relation to the typical value for silica FBGs that is 10 pm/°C (NEEHARIKA; PATTNAIK, 2015). The sensors on the claws center are surrounded by a similar volume of material and for this reason, they have sensitivities close to each other. On other hand, the temperature compensation FBG on the lateral face of the claws is under a small PLA piece and presents lower sensitivity compared to the others for both claws of the first design. The temperature sensitivity differences between claws may be related to the different volumes of epoxy resin deposited in the surface slot of each claw. Nevertheless, it is still possible to compensate for the effects of temperature on optical strain gauges by knowing all the sensitivities.

Figure 29 show the points collected during the temperature experiments and the respective linear fitted models for each FBG of the left and right sides of the second design

of the claws.

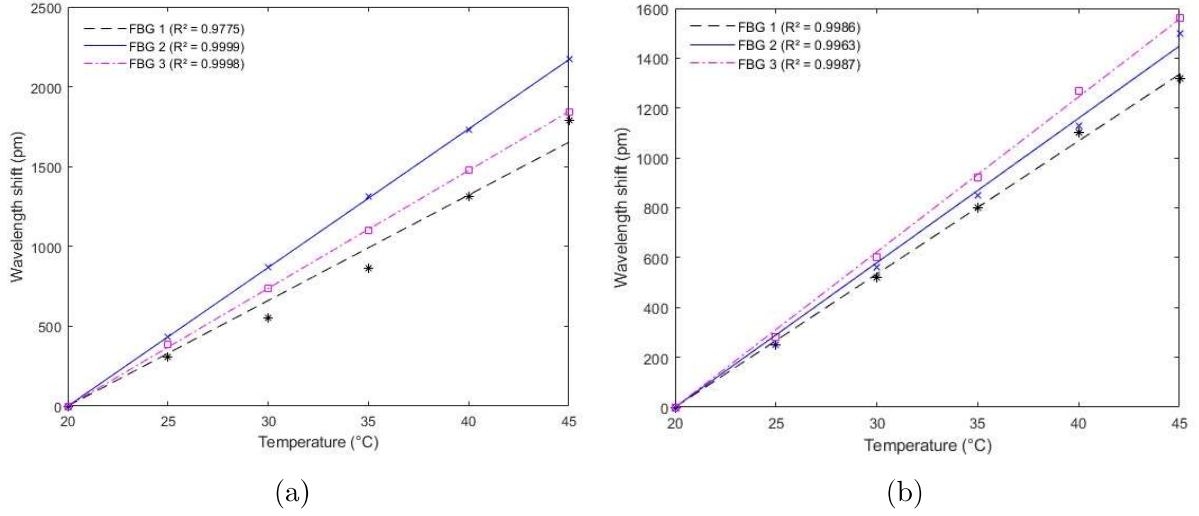


Figure 29 – Temperature characterization of the FBGs from the second design for (a) left claw and (b) right claw.

The wavelength shift of the sensors from both claws exhibited a highly linear behavior to temperature variations. This can be proved by seeing that the values of  $R^2$  are almost all equal to 1. The mean temperature sensitivity of the sensors of this design was relatively lower than the ones from the first design. In this case, there is a smaller amount of embedding material in contact with the FBGs and, consequently, their thermal expansion and the strain induced in the FBGs tend to be smaller than in the first project.

#### 4.1.3 Strain characterization

The points with error bars and the respective linear fitting curve for the strain characterization experiments of the first design of the claws can be seen in Figure 30.

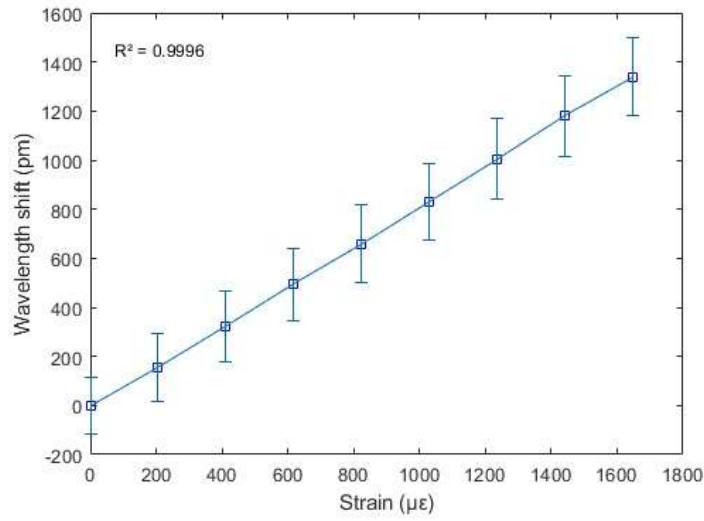


Figure 30 – Characterization of the reference FBG relative to strain for the claws first design.

The value of  $R^2$  for the linear regression shows that the sensor has a highly linear behavior to strain the sensor. Even though the behavior was linear, the sensitivity was different from the expected values of  $1.2 \text{ pm}/\mu\epsilon$  for silica FBGs (WEBB, 2015). As FBG is inside the epoxy resin, the resin's stiffness makes it difficult to deform the sensor and the strain transmitted to it tends to be smaller. The obtained sensitivity was equal to  $0.81 \pm 0.04 \text{ pm}/\mu\epsilon$ . The analysis of the results shows that the standard deviation values represent only about 0.001 percent of the values obtained for the wavelengths shifts indicating high repeatability of the tests. Due to the inaccuracies of manual manufacturing processes, it is known that the FBGs in the claws can be overlapped by different volumes of resin and approximating their sensitivity to strain with an auxiliary FBG may result in errors.

Figures 31 and 32 show the collected points with error bars and linear adjustment curve for each FBG of the left and right claws of the second design, respectively. The obtained sensitivity for each FBG may also be seen in the figures.



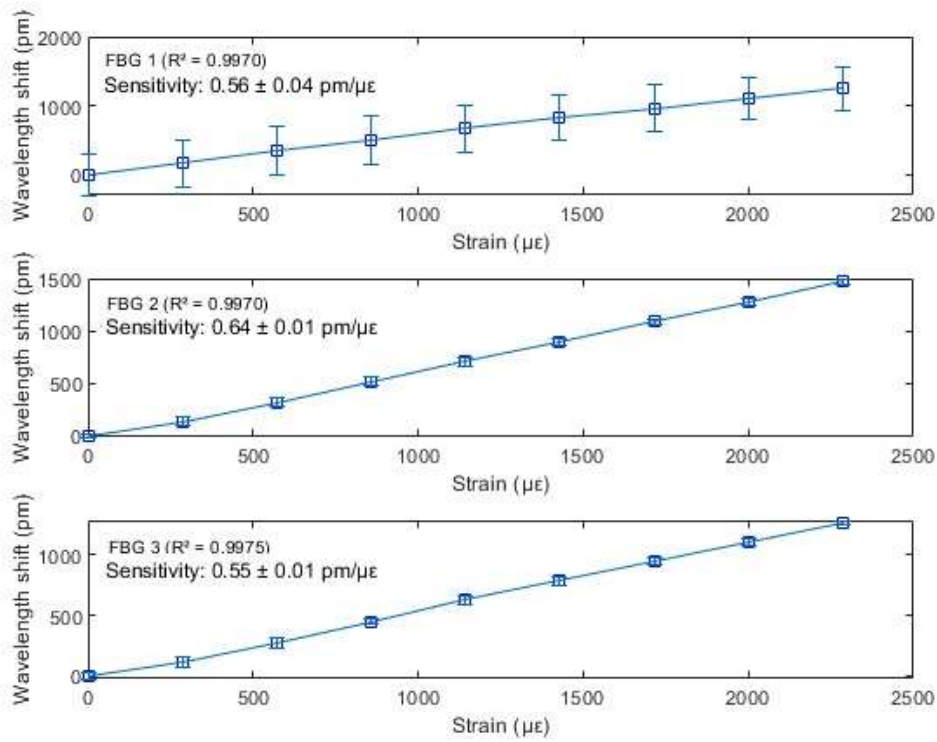


Figure 31 – Characterization relative to strain of the FBGs for left claw of second design

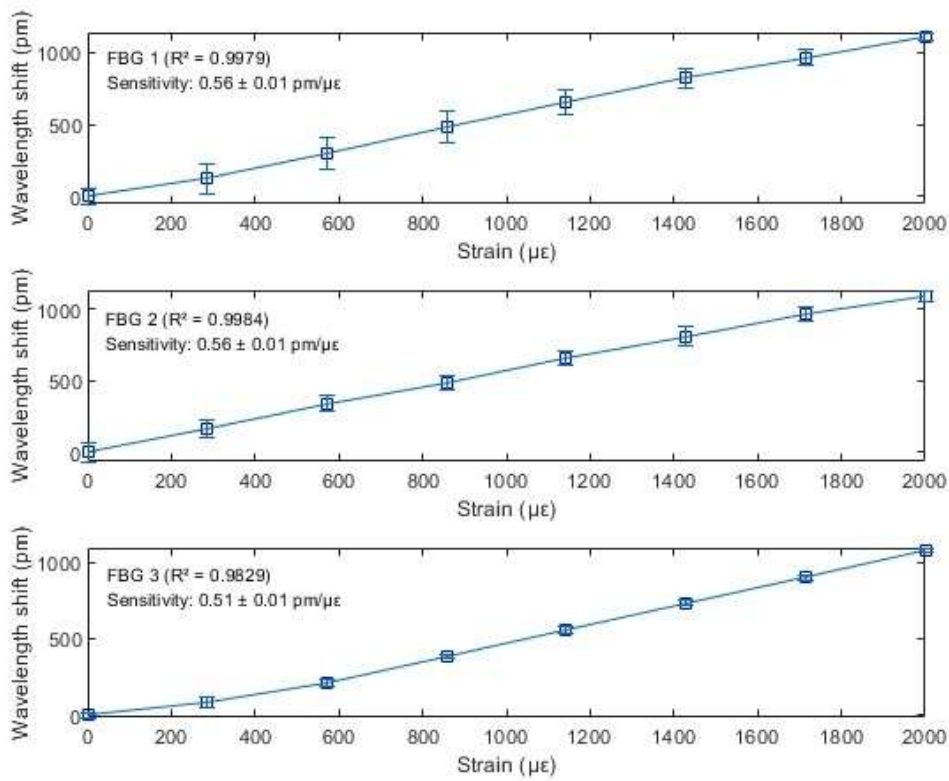


Figure 32 – Characterization relative to strain of the FBGs for right claw of second design.

The sensors exhibited a highly linear deformation response as shown by  $R^2$  values greater than 0.98. The base of the sensor was made of PLA, which is a more rigid material

than epoxy resin and therefore the sensitivity to strain of the sensors was smaller than that of the ones on the first prototype of the claws. In addition, the lower sensitivity indicates that the second design has a higher dynamic range than the first design being suitable for manipulators with higher load capacity. The differences in sensitivity between the claws of this project are related to the difficulty of positioning the FBGs exactly in the base center and ensuring that the glue points are at the same distance from the center. Again, it is not possible to control the epoxy resin that is positioned over each sensor. Since it was possible to carry out the strain characterization in the sensors that would be in the claw and not in an auxiliary sensor, it is expected that the measurements in the new prototype are more consistent and accurate.

The small differences in sensitivity to strain and temperature between the FBGs may be related to inaccuracies in the manufacturing process. Variations in 3D prints and manual positioning of cyanoacrylate and epoxy resin on the claws can result in parts with different finishes and consequently in different amounts of embedding material around each sensor.

#### 4.1.4 Compression tests

Figure 33 present the strain values for each load value applied on compression test for left and right claws of the first prototype. The calibration curve from Figure 30 was used to obtain the strain values from the wavelength shifts for each FBG.

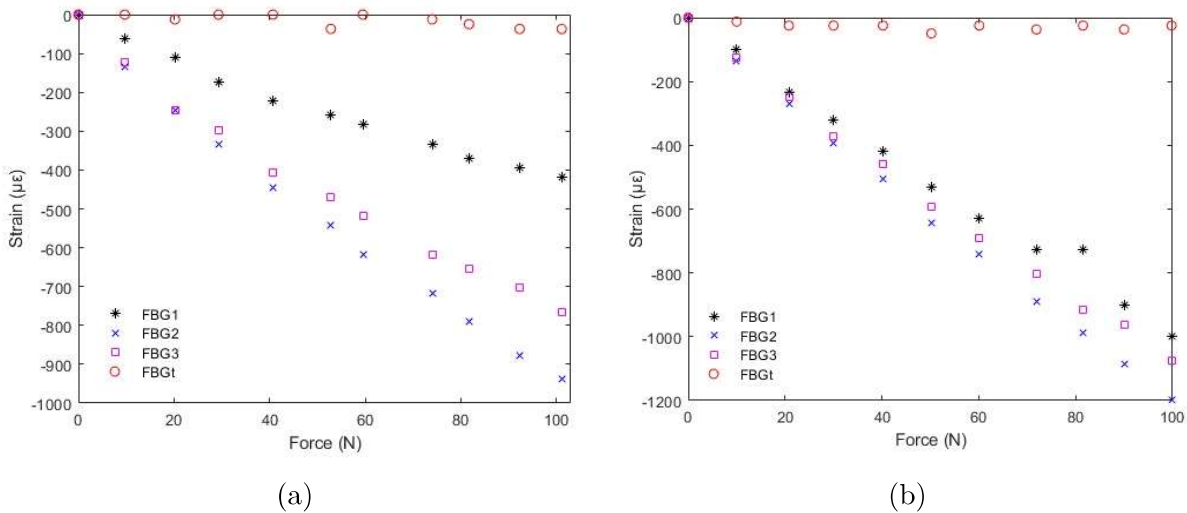


Figure 33 – Strain values for compression test on the first design for (a) left claw and (b) right claw.

The results show an almost linear response for all load values applied to the three FBGs in both claws with  $R^2$  values superior to 0.9567 for the left claw and 0.9898 for the right claw. Thus, it is known that the dynamic range of the sensors is suitable for load values of at least 100N at the center of the claws. Misalignment of the claw on the

machine prior to starting the tests causes unequal loads on the FBGs which has as a result different values of strain for an applied force. The lower strain values obtained for the left claw when compared to the right claw are due to the uncontrolled manual deposition of a higher volume of epoxy resin in the claw slot which makes the region where the sensors are positioned more rigid. These differences reinforce the idea that characterization to strain with the auxiliary FBG can be a source of measurement errors.

Differently from the expected, the positive axial strains on the sensors were not achieved. For this reason, it is therefore assumed that the mechanical stresses on FBGs were not purely tractive. The analysis of the grating reflectivity, the direction of the wavelength shift and the full width half maximum (FWHM) is a way to estimate the nature of the type of force acting on the FBGs (LEAL-JUNIOR et al., 2019). In order to allow this evaluation, Figure 34 simultaneously shows the spectrum of the FBG 3, selected randomly, from the right claw relative to each applied load to check its behavior.

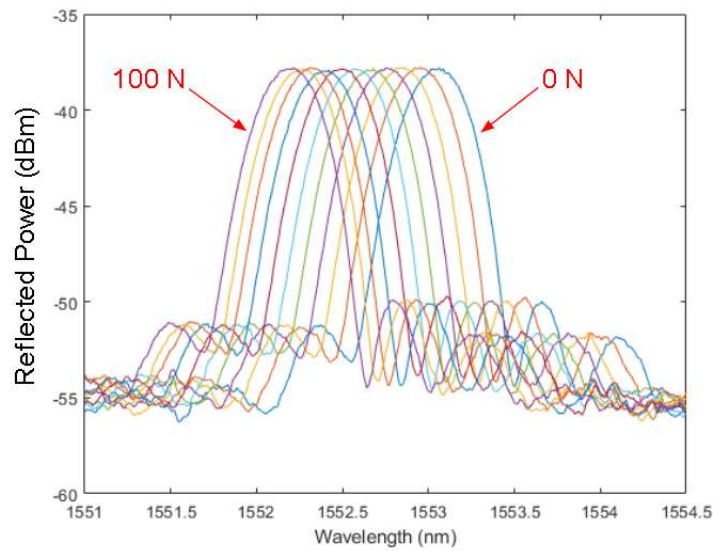


Figure 34 – Reflection spectrum of FBG 3 (right claw) under compressive load.

The graph shows that the signal shifts to lower wavelengths and it is hard to see changes in the grating reflectivity and the FWHM. As noted during the manufacturing process, with the proposed design it is not easy to control the positioning and ensure that the fiber is away from the walls and leaning against the bottom of the slot during the injection of the epoxy resin. This allows an amount of epoxy resin to settle under the fiber prior to the cure process and act as a flexible substrate onto which the silica fiber can bend. The bending prevents the transverse deformation of the fiber when it is being compressed against the PLA surface and the induction of a positive axial strain due to the Poisson Effect does not happen. It can be assumed then that the fiber is in the compressive region of the bending, nevertheless, the bending moments induced by the compression loads were not large enough to cause signal losses. Furthermore, as the sensors are contained in the same fiber, it may be possible that strain in one of the sensors is improperly transferred

to the other by fiber continuity and the results were affected. The obtained results show that the behavior of the numerical and experimental analyses are similar.

Figure 35 present the strain values for each load value applied on compression test for left and right claws of the second prototype. The calibration curves from Figures 31 and 32 were used to obtain the strain values from the wavelength shifts for each FBG of the left and right claws, respectively.

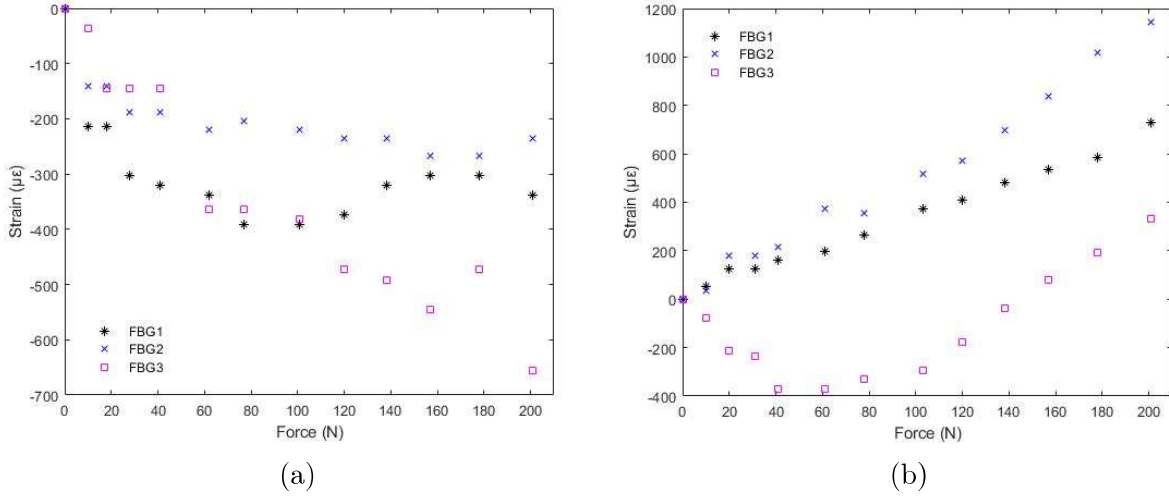


Figure 35 – Strain values for compression test on the second design for (a) left claw and (b) right claw.

In this case, it is expected that the optical fibers have a smaller space to bend due to the proposed design. As observed on the graphs, the left claw presented predominantly negative strains which indicate similar effects of bending that happened on the first claw. The fiber positioning on the bending compressive region results in negative values of stain on the FBGs, however when the fiber touches the bottom of the slots it starts to be compressed transversely against the claw. This transverse strain has as consequence a positive axial strain in the FBGs due to the Poisson effect. Thanks to the tradeoff between positive and negative strains, the data points follow a non-linear pattern and oscillate between increasing and decreasing values. On the right claw, an improvement in the quality of the 3D printing enabled a better fit of the sensor bases in the slots, preventing an empty space for the occurrence of bending. For this reason, the right claw showed predominantly linear positive results as a consequence of the Poisson effect.

The manufacturing process of this design has a set of variables to be controlled as the glue points on the claw, glue points of the fiber on the base, positioning of the FBGs in the base, glue volume and epoxy resin deposited on the sensors. As it is not guaranteed that all process steps are replicated identically for each sensor, it is expected that the sensor responses be considerably different from each other, as seen in the figures.

The first project of the claws was chosen for the tests on the robot since its sensors

presented linear behavior for both claws and a higher measurement range. The behavior of the sensors of the second project is highly random for loads values superior to 40 N and the tests indicated low repeatability of the second prototype of the claws.

#### 4.1.5 Experimental validation

In order for the robot to hold the object during the tests, it is necessary that the sum of the object's weight and the friction force between the claw and the object is zero. The friction force is proportional to the contact area of the surfaces' roughness and to the normal force existing at the contact. For the object to be in balance, it is hard to guarantee that contact with the claws happens always in the same region. For this reason, there is a variation in the effective contact area between tests and consequently in the normal force which corresponds to the clamping force of the claw. Internal forces tend to be greatest near the contact pressure region and a different map of internal forces in the grip body is expected for each test.

The claws are attached to the robot with screws and this induces a behavior similar to a clamped beam under bending when an object is picked up. Consequently, the region of the claw in which the sensors are positioned tends to experience normal tractive stresses while the opposite side is under the effect of compressive stresses due to gripping force. Furthermore, the compression tests done previously showed that pressure in the region close to the FBGs tends to induce compressive stresses in the sensors due to the space available for the fiber to bend in the claw slot. This combination of effects makes it possible for some sensors in the rosette to be under tractive stress while others to be under compressive stress in a single test. From these analyzes, it is assumed that the experiments are considerably dependent on the way the robot captures the object and, as it is difficult to have control over this parameter, the results are significantly different between tests. The polymeric materials that make up the claw structure exhibit viscoelastic behavior which makes their stress-strain response time-dependent. Thus, immediately after the gripping force is ceased the sensors still present a deformation due to the creep effect.

Table 3 and 4 present the principal normal stresses, maximum shear stress, and its orientation angles for the tests on the quadrangular prism and the cylinder. The results present a tradeoff between the compressive and tractive stresses previously mentioned. For the cases in which there are bigger negative values for the principal stresses is expected that the object has gripped near to the sensors region on the claws center and the strains induced by bending were higher. On the other hand, for the cases that predominated positive stresses, the flexion of the claw structure produced greater strains than the compression strains of the epoxy resin bending, since these were lower due to the pressure farther from the claw center.

Table 3 – Results of the tests on the quadrangular prism.

	Left Claw			Right Claw		
	Test 1	Test 2	Test 3	Test 1	Test 2	Test 3
Maximum Stress (Pa)	0	0	0	0	0	0
	-131.05	59.95	-298.40	38.22	-67.35	186.92
	-106.48	81.98	-19.81	-17.66	61.65	156.68
Minimum Stress (Pa)	0	0	0	0	0	0
	-193.10	-39.70	-385.36	-162.30	-277.06	73.91
	-217.67	-23.73	-243.56	-53.25	-61.64	61.11
Angle Principal Stresses (°)	0	0	0	0	0	0
	-18.29	30.00	-18.52	21.28	-35.08	-0.39
	43.16	33.35	-34.76	30.00	15.00	25.36
Maximum Shear Stress (Pa)	0	0	0	0	0	0
	31.03	49.83	43.48	100.26	104.86	56.51
	55.59	52.86	111.87	17.79	61.65	47.78
Angle Max Shear Stress (°)	0	0	0	0	0	0
	26.70	-15.00	26.47	-23.72	9.92	44.61
	-1.83	-11.65	10.24	-15.00	-30.00	-19.64

Table 4 – Results of the tests on the cylinder.

	Left Claw			Right Claw		
	Test 1	Test 2	Test 3	Test 1	Test 2	Test 3
Maximum Stress (Pa)	0	0	0	0	0	0
	76.31	167.28	132.13	323.60	137.44	-37.52
	69.48	191.26	202.67	143.15	263.52	75.28
Minimum Stress (Pa)	0	0	0	0	0	0
	24.98	96.10	-91.61	81.59	-96.92	-225.85
	31.82	107.57	-40.60	-1.33	-0.14	-176.58
Angle Principal Stresses (°)	0	0	0	0	0	0
	-36.95	-30.00	11.34	-30.00	15.87	-39.55
	39.55	31.05	27.09	34.91	-9.55	25.77
Maximum Shear Stress (Pa)	0	0	0	0	0	0
	25.66	35.59	111.87	121.01	117.18	94.16
	18.83	41.85	121.63	72.24	131.83	125.93
Angle Max Shear Stress (°)	0	0	0	0	0	0
	8.05	15.00	-33.65	15.00	-29.13	5.44
	-5.44	-13.94	-17.91	-10.08	35.45	-19.22

Since the FBGs are embedded in the epoxy resin, any deformation suffered by the resin is transferred to the sensors. Therefore, it is assumed that the resin is under the same strain values that are obtained from the FBG data. It is possible to use the equations of the theoretical background and the mechanical properties of the epoxy resin to discover the mechanical stresses on its structure during the tests.

In the claws experiments on the robot, the maximum force value which can be applied by the used gripper is insufficient to cause permanent deformations on the claw structure. However, knowing the information obtained from the sensors it is possible to assess whether the structure material is at risk by applying some failure criteria for ductile materials and thereby preserving the structural integrity of the robot work tool. Since the analysis must be carried out for the embedding material, the stress values obtained in

Table 3 and 4 are in the order of Pa and, which are low when compared with epoxy resin yield strength.

## 4.2 Tactile system's experimental results

### 4.2.1 Temperature and force characterization

Figure 36 show the linear models fitted from the points collected during the temperature characterization for each FBG in the smart textiles from links 1 to 4, respectively.

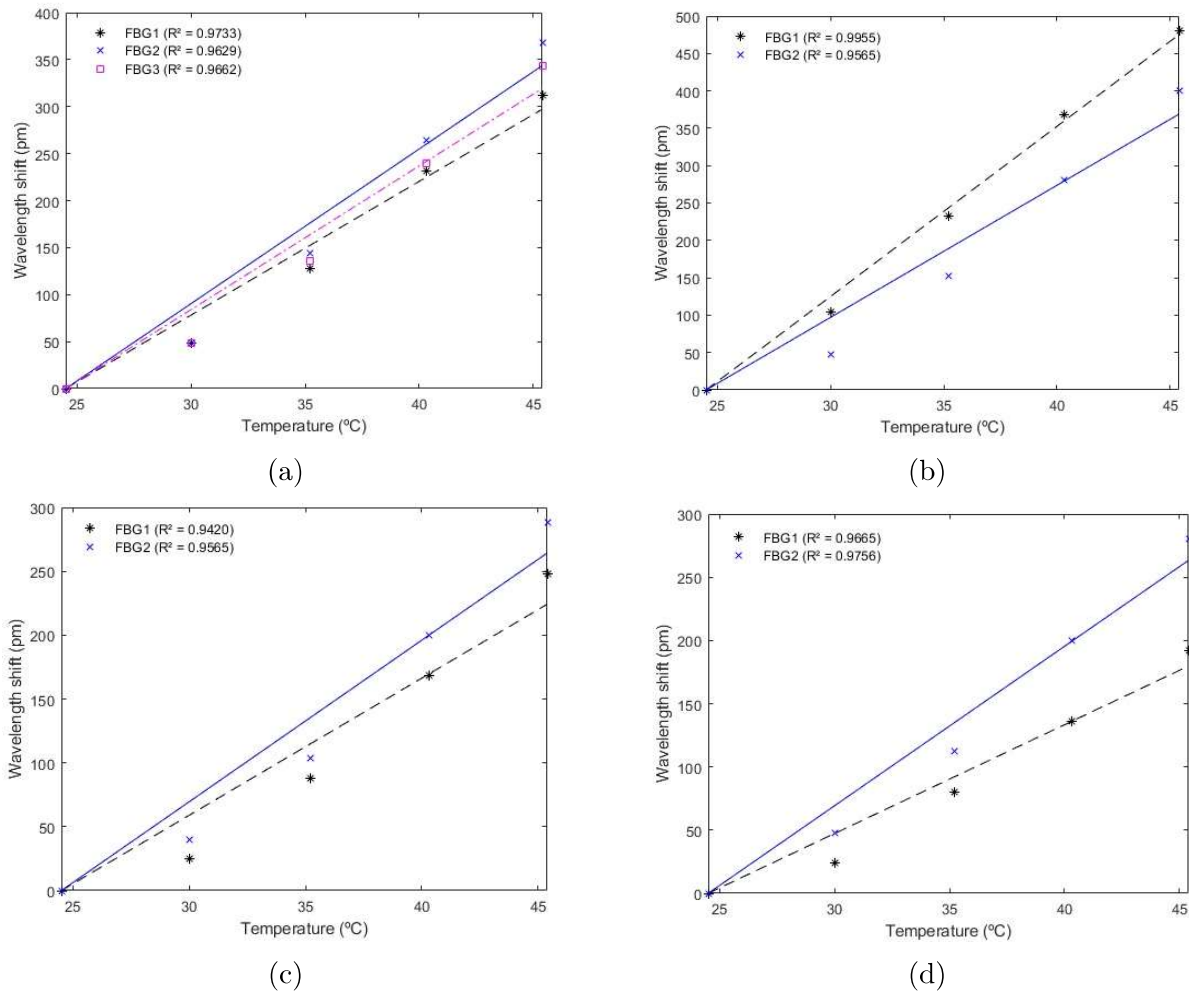


Figure 36 – Temperature characterization of smart textiles in relation to (a) link 1, (b) link 2, (c) link 3 and (d) link 4.

For information obtained from the compression tests, Figure 37 shows the characterization of each of the sensors that make up the smart textiles of links 1 to 4, respectively.



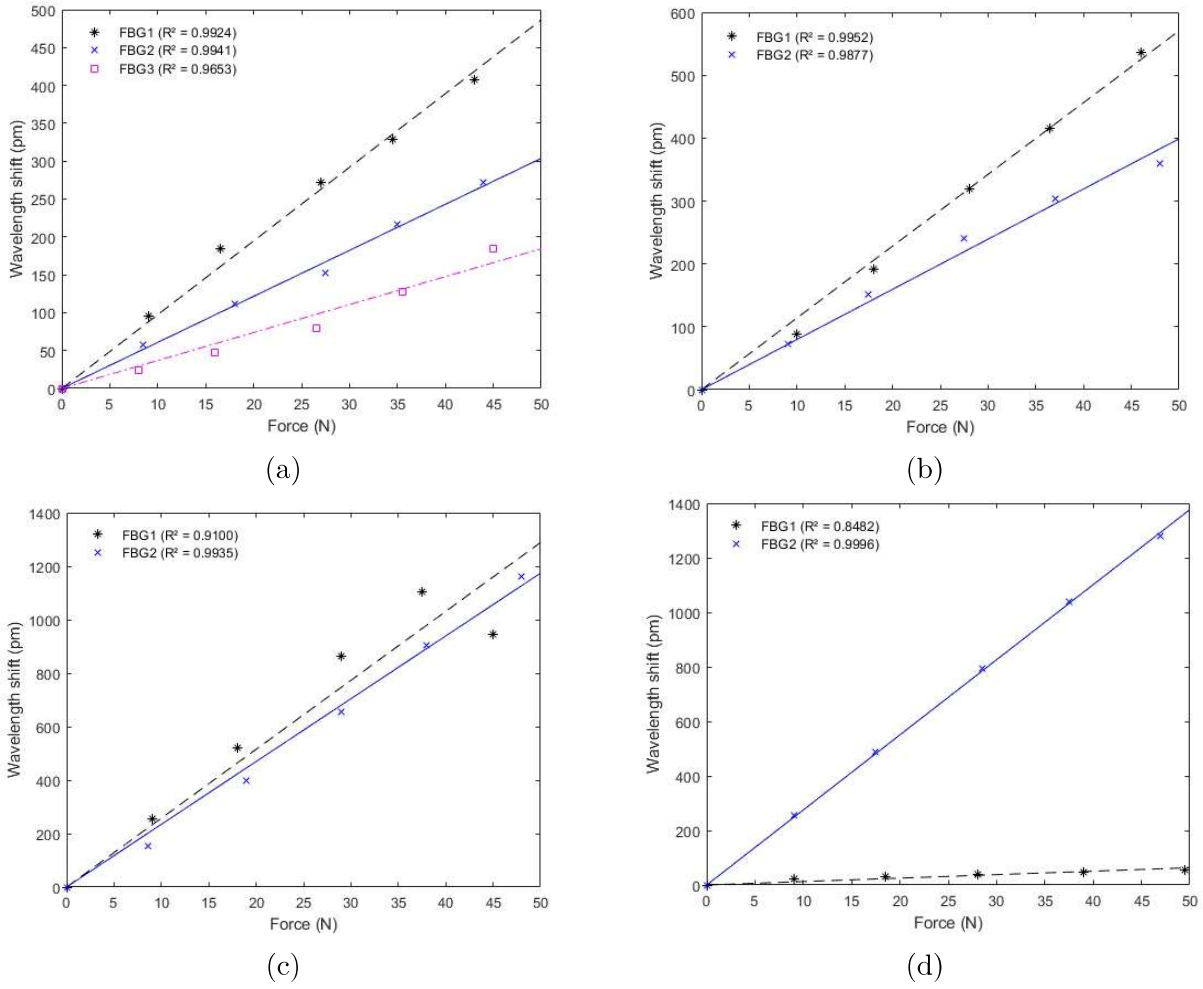


Figure 37 – Force characterization of smart textiles in relation to (a) link 1, (b) link 2, (c) link 3 and (d) link 4.

Table 5 presents the sensitivities relative to temperature and force of all sensors according to the convention of Figure 23.

Table 5 – Sensitivities of the tactile system sensors.

Link	Sensor	Temperature sensitivity (pm/°C)	Force sensitivity (pm/N)
Link 1	FBG 1	14.22	9.73
	FBG 2	16.44	6.07
	FBG 3	15.28	3.69
Link 2	FBG 1	22.74	11.41
	FBG 2	17.65	7.97
Link 3	FBG 1	10.73	25.77
	FBG 2	12.65	23.48
Link 4	FBG 1	8.60	1.26
	FBG 2	12.60	27.53

Temperature characterization is relevant for situations where the robot operates in environments with temperature fluctuations. In this way, the strategy proposed in Eq. 2.41 can be used to avoid cross-sensitivity of temperature with the parameter of interest.



However, since a thermal plant exhibits a slow time response, it may be easy to separate the impact response on the sensors from the temperature response by this difference in frequencies.

As the manufacturing process of the sensing system is carried out manually, the sensitivity of the sensors is expected to vary significantly from one to the other as can be seen in Table 5. For the supports of the sensors containing a higher volume of silicone rubber, it is expected a higher thermal expansion of the material which tends to cause greater deformations in the sensors. For this reason, when the volume of silicone in the support is greater is expected higher temperature sensitivity is expected more temperature-sensitive sensors. In relation to force, a small deformation is expected for a high volume of material, since the stiffness of the material is greater when the volume is high. Consequently, sensors with more silicone tend to be less force sensitive.

For FBGs where there is an excess of silicone volume in relation to the available volume of the support, the material that overflows tends to form a convex-shaped surface due to the effect of superficial tension before the cure of the material. Due to the curvature of the surface, it is difficult to ensure that the load is applied perpendicular to the silicone surface. For this reason, in some cases, the force may have been applied obliquely to the upper surface of the support and interfered with the sensitivity value.

Linear regression was used to obtain the relation between temperature variation and force with the central wavelength shift on the FBGs. Almost all the lines which are shown in Figures 36 and 37 have a coefficient of determination  $R^2$  greater than 0.94 which indicates a significantly linear behavior. The  $R^2$  lower than 0.94 of some curves is directly related to outliers on the data. The last point collected for FBG 1 on link 3 presented a smaller wavelength shift than the penultimate point. For this case, the sensor support may have been moving at the base of the machine so that the load was not applied at its center. If the load was applied to a more rigid region, such as the 3D printed support, then the sensor would experience less deformation and, consequently, a smaller wavelength shift. A similar approach can be considered for the high wavelength shift difference between the first and second points of FBG 1 on link 4.

Compared to the other sensors, the lower sensitivity to temperature and force of FBG 1 on link 4 may be related to the volume of silicone rubber positioned on its 3D printed support. It is assumed that the volume of silicone rubber was insufficient to fully embed the sensor and fill the support. The compressive force of the characterization is then applied directly to the support, which is more rigid than the silicone rubber and consequently, the sensitivity of this FBG tends to be lower. The incomplete embedding of this FBG prevents the thermal expansion of the silicone from causing the same level of deformation that occurs in other sensors and consequently, reduces its sensitivity to temperature.

### 4.2.2 Experimental validation

For analysis of the tactile system, Figure 38 presents the behavior of some FBGs on the links 1 to 4 for one test without external perturbation.

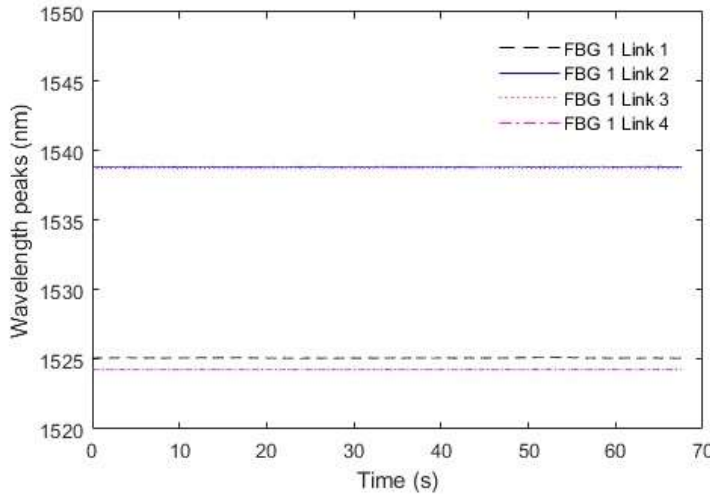


Figure 38 – Sensors response during the test of the tactile system without external perturbations.

As can be seen in Figure 38, during the movements without external perturbations the central wavelength of the FBGs remains approximately constant. Figure 38 shows this behavior only for some of the FBGs, however it happens for all others. As the FBGs are positioned over the robot's links, they tend to behave similarly to a rigid body and do not deform during movement. If an optical fiber were shared by two different links, the FBGs contained in it would present a variation in their central wavelength due to the change in the joint angle that joins the links. This avoids the need for complex signal processing algorithms to separate responses of different sources in the reflection spectrum. The non-abrupt variations in the signal observed between 50 s and 55 s for the FBG 1 on link 3 were due to the textile moving slightly in the links.

Figure 39 presents the behavior of the FBGs in the links 1 to 4 with higher values of wavelength shifts due to the impacts on the left side of the robot's body.

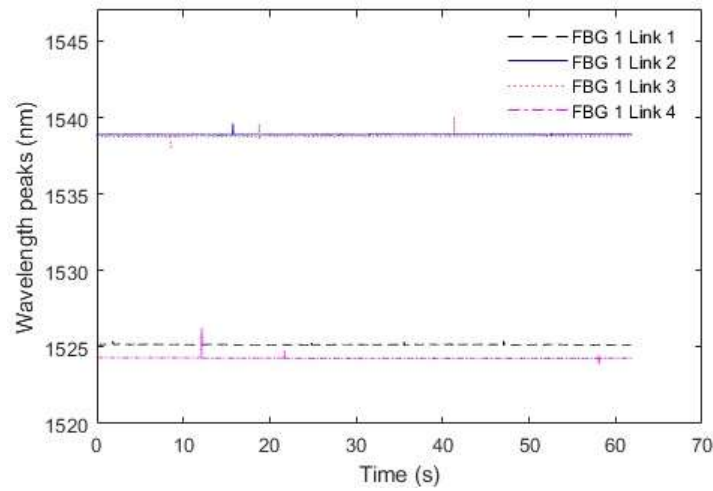


Figure 39 – Sensors response during the test with hits on the left side of the robot's body.

The FBGs 1 of each link were the ones that detected higher wavelength shifts for the tests with impacts on the left side of the robot. For this type of test, it is not possible to compare qualitatively the FBGs in terms of sensitivity to force. This difficulty arises from the fact that the human operator of the rubber mallet has no control over the force he applies on impact. However, using the force characterization obtained for the sensors in 37, it is possible to estimate the intensity of the impacts in terms of force.

Figure 40 presents the behavior of the FBGs in the links 1 to 4 with higher values of wavelength shifts due to the impacts on the front side of the robot's body. The time instants at which the FBGs in the figure has a high wavelength shift are presumably related to interference and errors in data collection and not related to impacts.

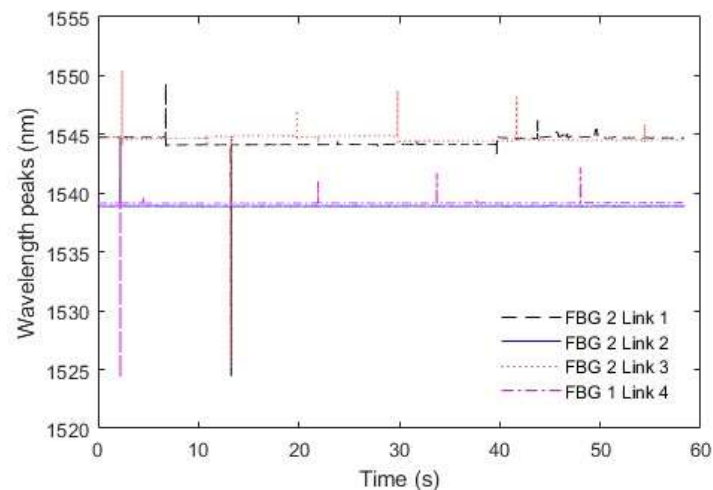


Figure 40 – Sensors response during the test with hits on the front side of the robot's body.

The FBGs 2 of each link were the ones that detected higher wavelength shifts for the tests with impacts on the lateral side of the robot. Depending on the force of the applied

impact, the others FBGs in the optical fiber also suffer deformation and consequently a wavelength shift at the moment of the impact. If the impact occurs between two adjacent sensors, it is not possible to determine the exact point which it hit. For this reason, to amplify the spatial resolution of the system, it's necessary to increase the number of FBGs in each optical fiber.

The wavelength shift tends to be small for FBGs further away from the impact site. For this situation, it is possible to identify the impacts and the moments they occur from at least one of the peaks data from an optical fiber detected by the interrogator. This approach was used for link 4 as can be seen in Figure 40. The spectrum signal of the optical fiber on link 4 presented high attenuation presumably due to the low quality of the used optical cables and this prevented the interrogator from detecting the peaks of the FBG 2. For this reason, FBG 1 was used in the procedure of impact detection for link 4.

From these results, the proposed tactile sensing system proved itself feasible to detect external interferences from the environment which can compromise the performance of the manipulator in service. Using the system is possible to detect the magnitude in terms of force, the instant of time and position on the robot body in which the impact happened.

This system can be implemented together with an impedance control or other control strategy to make the industrial environment safer, especially in collaborative tasks with human beings. This is done by controlling the speed at which the robot must move and the times at which it must stop moving.

## 5 Conclusions and future works

Monitoring the integrity of the structure of an equipment consists of a strategy to prolong its life in service without the need for unplanned downtime for corrective maintenance. However, predicting the stresses and strain states of complex geometries through analytical models or numerical simulations can still bring some errors in the results and lead to a mistaken posture. Human-robot interaction to perform a specific task ensures an environment in which the resource use effectiveness and productivity can be improved by combining robots characteristics with flexibility and dexterity of humans in dealing with unexpected and non-repetitive tasks.

Low-level control strategies alone are usually insufficient for the robot to develop group tasks with humans. For that reason, robots with amplified tactile sensitivity combined with modern control strategies make the work environment safer for human collaborators.

This dissertation developed FBG-based experimental strategies to monitor the tool's structural integrity and to improve the tactile sensitivity of a robotic manipulator during operation. The choice for FBG-based sensors was mainly due to their advantages of use for the application and in robotic devices such as multiplexing capability, immunity to electromagnetic noise and availability of established commercial equipment to monitor the sensors' reflection spectrum. The FBGs were fabricated in silica optical fibers using the technique of the inscription with pulsed laser and phase mask.

The chosen design for instrumented claws is equipped with sensors that exhibit a highly linear behavior to temperature and strain stimuli. Moreover, this behavior remained linear for load values greater than 100 N, showing that the dynamic range of the sensors is feasible at the load limits of the used gripper and ensures that the instrumented claws can be applied in situations that require higher force capacities. A FEM analysis was used as a strategy to prove the bending nature of the shifts to lower wavelengths obtained in the compression experiments. A strategy that decouples the effects of strain and temperature on Bragg wavelength shift was proposed to compensate for the temperature effects on the FBGs by using an additional FBG on the body of each claw. Even though the strain characterization tests proved that the sensors presented high repeatability (standard deviation of 0.001 percent for the wavelength shifts), the results of the tests on the robot were significantly different from each other. The existence of some uncontrollable variables such as position, orientation, and surface roughness of the object and the robot holding the object at the same points hinder an identical replication of the experiment and the results cannot be related to the performance of the sensors which was positive in the static tests. The instrumented gripper is then viable to obtain critical stresses and strains and

to verify, applying failure criteria, if the equipment is at risk.

The tactile system consists of FBG-based smart textiles installed on the robot's links. A mathematical model was proposed to estimate the distance of the sensors that guarantee the largest sensitive area for the system. After fabrication, the sensors were characterized in terms of force and temperature so that it was possible to implement the strategy to avoid cross-sensitivity effects, similar to the instrumented claws. The relation between force and temperature and Bragg wavelength shift showed a highly linear behavior (almost all  $R^2$  superior to 0.94). As expected, the tactile system was not sensitive to the robot's movement and for this reason, complex processing algorithms were not necessary to separate the part of the signal related to external interference. From the results of the validation experiments, the system proved to be efficient in detecting the position and intensity of external impacts in real-time and to be a feasible alternative to work together with a performance improvement control system.

For future works, it is suggested to develop a configuration for the sensors that allow the monitoring of the strain map along the entire claw surface. As the mechanical forces on the tool are dependent on some parameters that are difficult to control such as the object geometry, the contact area between tool and object, the position and orientation of the object when being gripped and the roughness of the surfaces, this strategy becomes relevant since it is not possible to guarantee the critical region on the tool is located at its center. Thus, the multiplexing capability of FBGs allows using a single optical fiber to spread sets of rosettes along with the claw. Another suggestion is to design an instrumented tool to similarly monitor processes with higher loads such as the machining and effectively assess the mechanical structural limitation of sensors or the welding in which temperature compensation algorithms become relevant due to the high thermal input of the process. In terms of the tactile system, it is suggested to use a portable multiplexing approach to extend the strategy to other types of robots, such as mobile or humanoid robots. The intensity variation-based sensors with a multiplexing technique have compact and lightweight components making them a possible solution for this approach.

# Bibliography

ABANG, A.; WEBB, D. J. Demountable connection for polymer optical fiber grating sensors. *Optical Engineering*, International Society for Optics and Photonics, v. 51, n. 8, p. 080503, 2012. Citado na página 40.

ACKERLEY, R. et al. Touch perceptions across skin sites: differences between sensitivity, direction discrimination and pleasantness. *Frontiers in behavioral neuroscience*, Frontiers, v. 8, p. 54, 2014. Citado na página 57.

ADDANKI, S.; AMIRI, I. S.; YUPAPIN, P. Review of optical fibers-introduction and applications in fiber lasers. *Results in Physics*, Elsevier, v. 10, p. 743–750, 2018. Citado na página 36.

BAHRIN, M. A. K. et al. Industry 4.0: A review on industrial automation and robotic. *Jurnal Teknologi*, v. 78, n. 6-13, 2016. Citado na página 21.

BANDARI, N.; DARGAHI, J.; PACKIRISAMY, M. Tactile sensors for minimally invasive surgery: a review of the state-of-the-art, applications, and perspectives. *IEEE Access*, IEEE, v. 8, p. 7682–7708, 2019. Citado na página 23.

BARRIAS, A. et al. Application of distributed optical fiber sensors for the health monitoring of two real structures in barcelona. *Structure and Infrastructure Engineering*, Taylor & Francis, v. 14, n. 7, p. 967–985, 2018. Citado na página 37.

BEER, F. P. et al. *Statics and Mechanics of Materials*. [S.l.]: McGraw-Hill Education New York, NY, USA, 2017. Citado 2 vezes nas páginas 31 and 32.

BETZ, D. C. et al. Advanced layout of a fiber bragg grating strain gauge rosette. *Journal of lightwave technology*, IEEE, v. 24, n. 2, p. 1019–1026, 2006. Citado na página 38.

CACHADA, A. et al. Maintenance 4.0: Intelligent and predictive maintenance system architecture. In: IEEE. *2018 IEEE 23rd international conference on emerging technologies and factory automation (ETFA)*. [S.l.], 2018. v. 1, p. 139–146. Citado na página 22.

CHELLADURAI, H.; JAIN, V.; VYAS, N. Development of a cutting tool condition monitoring system for high speed turning operation by vibration and strain analysis. *The International Journal of Advanced Manufacturing Technology*, Springer, v. 37, n. 5, p. 471–485, 2008. Citado na página 23.

CRAIG, J. J. *Introduction to robotics: mechanics and control, 3/E*. [S.l.]: Pearson Education India, 2009. Citado 4 vezes nas páginas 13, 27, 28, and 29.

DIAZ, C. A. et al. Optical fiber sensing for sub-millimeter liquid-level monitoring: a review. *IEEE Sensors Journal*, IEEE, v. 19, n. 17, p. 7179–7191, 2019. Citado 2 vezes nas páginas 36 and 38.

DÍAZ, C. A. et al. Liquid level measurement based on fbg-embedded diaphragms with temperature compensation. *IEEE Sensors Journal*, IEEE, v. 18, n. 1, p. 193–200, 2017. Citado 2 vezes nas páginas 39 and 57.

- DUMAS, C. et al. Joint stiffness identification of industrial serial robots. *Robotica*, Cambridge University Press, v. 30, n. 4, p. 649–659, 2012. Citado na página 30.
- ECKE, W. et al. Fibre optic sensor network for spacecraft health monitoring. *Measurement Science and Technology*, IOP Publishing, v. 12, n. 7, p. 974, 2001. Citado na página 37.
- FARAH, S.; ANDERSON, D. G.; LANGER, R. Physical and mechanical properties of pla, and their functions in widespread applications—a comprehensive review. *Advanced drug delivery reviews*, Elsevier, v. 107, p. 367–392, 2016. Citado na página 45.
- GASSERT, R.; DIETZ, V. Rehabilitation robots for the treatment of sensorimotor deficits: a neurophysiological perspective. *Journal of neuroengineering and rehabilitation*, BioMed Central, v. 15, n. 1, p. 1–15, 2018. Citado na página 22.
- GE, J. et al. Spiral-structured fiber bragg grating for contact force sensing through direct power measurement. *Optics express*, Optical Society of America, v. 22, n. 9, p. 10439–10445, 2014. Citado na página 38.
- HILL, K. O. et al. Photosensitivity in optical fiber waveguides: Application to reflection filter fabrication. *Applied physics letters*, American Institute of Physics, v. 32, n. 10, p. 647–649, 1978. Citado na página 38.
- HILL, K. O.; MELTZ, G. Fiber bragg grating technology fundamentals and overview. *Journal of lightwave technology*, IEEE, v. 15, n. 8, p. 1263–1276, 1997. Citado 2 vezes nas páginas 37 and 39.
- HILLBRICK, L. K. et al. Determination of the transverse modulus of cylindrical samples by compression between two parallel flat plates. *SN Applied Sciences*, Springer, v. 1, n. 7, p. 1–11, 2019. Citado na página 57.
- IRIARTE, X. et al. Optimal strain-gauge placement for mechanical load estimation in circular cross-section shafts. *Measurement*, Elsevier, v. 174, p. 108938, 2021. Citado na página 23.
- JAIN, T.; KALER, R. *Performance Investigation of Fiber Bragg Grating Temperature Sensor for Industrial Application*. Tese (Doutorado), 2018. Citado na página 37.
- JASCHINSKI, T. et al. Laparoscopic versus open surgery for suspected appendicitis. *Cochrane Database of Systematic Reviews*, John Wiley & Sons, Ltd, n. 11, 2018. Citado na página 23.
- JOE, H.-E. et al. A review on optical fiber sensors for environmental monitoring. *International journal of precision engineering and manufacturing-green technology*, Springer, v. 5, n. 1, p. 173–191, 2018. Citado na página 37.
- KERSEY, A. D. et al. Fiber grating sensors. *Journal of lightwave technology*, IEEE, v. 15, n. 8, p. 1442–1463, 1997. Citado na página 23.
- KUMAR, A. et al. Design studies and optimization of position of strain gauge. *Int. J. Sci. Eng. Res.*, v. 3, p. 1–4, 2012. Citado na página 30.
- LACRAZ, A. et al. Femtosecond laser inscribed bragg gratings in low loss cytop polymer optical fiber. *IEEE Photonics Technology Letters*, IEEE, v. 27, n. 7, p. 693–696, 2015. Citado na página 38.



LANGER, A. et al. Trust in socially assistive robots: Considerations for use in rehabilitation. *Neuroscience & Biobehavioral Reviews*, Elsevier, v. 104, p. 231–239, 2019. Citado na página 22.

LEAL-JUNIOR, A. et al. Smart textiles for multimodal wearable sensing using highly stretchable multiplexed optical fiber system. *Scientific Reports*, Nature Publishing Group, v. 10, n. 1, p. 1–12, 2020. Citado na página 24.

LEAL-JUNIOR, A. et al. Polymer optical fiber-based integrated instrumentation in a robot-assisted rehabilitation smart environment: A proof of concept. *Sensors*, Multidisciplinary Digital Publishing Institute, v. 20, n. 11, p. 3199, 2020. Citado na página 23.

LEAL-JUNIOR, A. et al. Application of additive layer manufacturing technique on the development of high sensitive fiber bragg grating temperature sensors. *Sensors*, Multidisciplinary Digital Publishing Institute, v. 18, n. 12, p. 4120, 2018. Citado na página 38.

LEAL-JUNIOR, A. G. et al. Multiplexing technique for quasi-distributed sensors arrays in polymer optical fiber intensity variation-based sensors. *Optics & Laser Technology*, Elsevier, v. 111, p. 81–88, 2019. Citado na página 37.

LEAL-JUNIOR, A. G. et al. Design considerations, analysis, and application of a low-cost, fully portable, wearable polymer optical fiber curvature sensor. *Applied optics*, Optical Society of America, v. 57, n. 24, p. 6927–6936, 2018. Citado na página 37.

LEAL-JUNIOR, A. G. et al. Development of polymer optical fiber sensors for lower limb exoskeletons instrumentation. In: SPRINGER. *International Symposium on Wearable Robotics*. [S.l.], 2018. p. 155–159. Citado 2 vezes nas páginas 23 and 24.

LEAL-JUNIOR, A. G. et al. Viscoelastic features based compensation technique for polymer optical fiber curvature sensors. *Optics & Laser Technology*, Elsevier, v. 105, p. 35–40, 2018. Citado na página 40.

LEAL-JUNIOR, A. G.; FRIZERA, A.; PONTES, M. J. Dynamic compensation technique for pof curvature sensors. *Journal of Lightwave Technology*, IEEE, v. 36, n. 4, p. 1112–1117, 2018. Citado na página 40.

LEAL-JUNIOR, A. G. et al. Fbg-embedded 3-d printed abs sensing pads: The impact of infill density on sensitivity and dynamic range in force sensors. *IEEE Sensors Journal*, IEEE, v. 18, n. 20, p. 8381–8388, 2018. Citado na página 37.

LEAL-JUNIOR, A. G. et al. Simultaneous measurement of axial strain, bending and torsion with a single fiber bragg grating in cytop fiber. *Journal of Lightwave Technology*, IEEE, v. 37, n. 3, p. 971–980, 2019. Citado na página 69.

LI, G. et al. Joint stiffness identification and deformation compensation of serial robots based on dual quaternion algebra. *Applied Sciences*, Multidisciplinary Digital Publishing Institute, v. 9, n. 1, p. 65, 2019. Citado na página 22.

LING, H.-Y. et al. Characterization of dynamic strain measurement using reflection spectrum from a fiber bragg grating. *Optics Communications*, Elsevier, v. 270, n. 1, p. 25–30, 2007. Citado na página 37.

- LUNDBERG, G.; YHLAND, E. *Cylinder compressed between two plane bodies*. [S.l.]: SKF, 1949. Citado na página 57.
- LUO, Y. et al. Fabrication of polymer optical fibre (pof) gratings. *Sensors*, Multidisciplinary Digital Publishing Institute, v. 17, n. 3, p. 511, 2017. Citado na página 38.
- MAGNE, S. et al. State-of-strain evaluation with fiber bragg grating rosettes: application to discrimination between strain and temperature effects in fiber sensors. *Applied optics*, Optical Society of America, v. 36, n. 36, p. 9437–9447, 1997. Citado na página 39.
- MARQUES, C. et al. Fast and stable gratings inscription in pofs made of different materials with pulsed 248 nm krf laser. *Optics express*, Optical Society of America, v. 26, n. 2, p. 2013–2022, 2018. Citado na página 38.
- NEEHARIKA, V.; PATTNAIK, P. K. Optical mems pressure sensors incorporating dual waveguide bragg gratings on diaphragms. *IEEE Sensors Journal*, IEEE, v. 16, n. 3, p. 681–687, 2015. Citado na página 64.
- OKAMURA, A. M. Haptic feedback in robot-assisted minimally invasive surgery. *Current opinion in urology*, NIH Public Access, v. 19, n. 1, p. 102, 2009. Citado 2 vezes nas páginas 22 and 30.
- OKAMURA, A. M.; MATARIĆ, M. J.; CHRISTENSEN, H. I. Medical and health-care robotics. *IEEE Robotics & Automation Magazine*, IEEE, v. 17, n. 3, p. 26–37, 2010. Citado na página 22.
- PETERS, K. Polymer optical fiber sensors—a review. *Smart materials and structures*, IOP Publishing, v. 20, n. 1, p. 013002, 2010. Citado 2 vezes nas páginas 23 and 37.
- PHAN, G.-H. et al. Estimating human wrist stiffness during a tooling task. *Sensors*, Multidisciplinary Digital Publishing Institute, v. 20, n. 11, p. 3260, 2020. Citado na página 22.
- PRISECARU, P. Challenges of the fourth industrial revolution. *Knowledge Horizons. Economics*, Dimitrie Cantemir Christian University, v. 8, n. 1, p. 57, 2016. Citado na página 21.
- QUANDT, B. M. et al. Body-monitoring and health supervision by means of optical fiber-based sensing systems in medical textiles. *Advanced healthcare materials*, Wiley Online Library, v. 4, n. 3, p. 330–355, 2015. Citado na página 23.
- RABBANI, M. J. et al. Model identification and validation for a heating system using matlab system identification toolbox. In: IOP PUBLISHING. *Iop conference series: Materials science and engineering*. [S.l.], 2013. v. 51, n. 1, p. 012022. Citado na página 49.
- ROMEO, L. et al. Internet of robotic things in smart domains: Applications and challenges. *Sensors*, Multidisciplinary Digital Publishing Institute, v. 20, n. 12, p. 3355, 2020. Citado na página 21.
- ROSSETTO, S.; BRAY, A.; LEVI, R. Three-dimensional strain rosettes: pattern selection and performance evaluation. *Experimental mechanics*, Springer, v. 15, n. 10, p. 375–381, 1975. Citado na página 31.

- SCHNEIDER, U. et al. Stiffness modeling of industrial robots for deformation compensation in machining. In: IEEE. *2014 IEEE/RSJ International Conference on Intelligent Robots and Systems*. [S.l.], 2014. p. 4464–4469. Citado na página 30.
- SCHOSTEK, S.; SCHURR, M. O.; BUESS, G. F. Review on aspects of artificial tactile feedback in laparoscopic surgery. *Medical engineering & physics*, Elsevier, v. 31, n. 8, p. 887–898, 2009. Citado na página 30.
- SHE, Y. et al. Exoskeleton-covered soft finger with vision-based proprioception and tactile sensing. In: IEEE. *2020 IEEE International Conference on Robotics and Automation (ICRA)*. [S.l.], 2020. p. 10075–10081. Citado na página 22.
- SHERWANI, F.; ASAD, M. M.; IBRAHIM, B. Collaborative robots and industrial revolution 4.0 (ir 4.0). In: IEEE. *2020 International Conference on Emerging Trends in Smart Technologies (ICETST)*. [S.l.], 2020. p. 1–5. Citado 2 vezes nas páginas 21 and 30.
- SICILIANO, B. et al. *Robotics: modelling, planning and control*. [S.l.]: Springer Science & Business Media, 2010. Citado 3 vezes nas páginas 13, 27, and 28.
- SONG, H.; KIM, K.; LEE, J. Development of optical fiber bragg grating force-reflection sensor system of medical application for safe minimally invasive robotic surgery. *Review of Scientific Instruments*, American Institute of Physics, v. 82, n. 7, p. 074301, 2011. Citado na página 24.
- SPONG, M. W. et al. *Robot modeling and control*. [S.l.]: wiley New York, 2006. v. 3. Citado na página 29.
- TAHIR, B. A. et al. Effect of sensor gauge length on strain sensitivity of a fiber bragg grating system. *Chinese Journal of Physics*, v. 49, n. 5, p. 1035–1045, 2011. Citado na página 58.
- THOBEN, K.-D.; WIESNER, S.; WUEST, T. “industrie 4.0” and smart manufacturing-a review of research issues and application examples. *International journal of automation technology*, Fuji Technology Press Ltd., v. 11, n. 1, p. 4–16, 2017. Citado 2 vezes nas páginas 21 and 22.
- VAIDYA, S.; AMBAD, P.; BHOSLE, S. Industry 4.0—a glimpse. *Procedia manufacturing*, Elsevier, v. 20, p. 233–238, 2018. Citado na página 21.
- WAGNER, C. R.; HOWE, R. D.; STYLOPOULOS, N. The role of force feedback in surgery: analysis of blunt dissection. In: CITESEER. *Haptic Interfaces for Virtual Environment and Teleoperator Systems, International Symposium on*. [S.l.], 2002. p. 73–73. Citado na página 23.
- WEBB, D. J. Fibre bragg grating sensors in polymer optical fibres. *Measurement Science and Technology*, IOP Publishing, v. 26, n. 9, p. 092004, 2015. Citado 2 vezes nas páginas 40 and 66.
- WERNECK, M. M. et al. A guide to fiber bragg grating sensors. *Current trends in short-and long-period fiber gratings*, InTech, p. 1–25, 2013. Citado na página 37.
- WIERZBA, P.; KOSMOWSKI, B. Application of polarisation-maintaining side-hole fibres to direct force measurement. *OPTOELECTRONICS REVIEW*, SIGMA NOT LTD, n. 4, p. 305–312, 2003. Citado na página 57.

XIONG, L. et al. A three-dimensional fiber bragg grating force sensor for robot. *IEEE Sensors Journal*, IEEE, v. 18, n. 9, p. 3632–3639, 2018. Citado na página 39.

YU, L. et al. Dual-core capacitive microfiber sensor for smart textile applications. *ACS applied materials & interfaces*, ACS Publications, v. 11, n. 36, p. 33347–33355, 2019. Citado na página 37.

ZIEMANN, O. et al. Pof handbook. *Springer*, Springer, 2008. Citado na página 36.